Analysis of Nerve Fibers and Their Distribution in Histologic Sections of the Human Brain

O. SCHMITT,[1]* M. PAKURA,[2] T. AACH,[2] L. HÖMKE,[3] M. BÖHME,[3] S. BOCK,[4] AND S. PREUßE[4]
[1]*Institute of Anatomy, University of Rostock, D-18055 Rostock, Germany*
[2]*Institute for Signal Processing, University of Lübeck, D-23569 Lübeck, Germany*
[3]*Institute of Mathematics, University of Lübeck, D-23560 Lübeck, Germany*
[4]*Institute of Anatomy, University of Lübeck, D-23560 Lübeck, Germany*

KEY WORDS nerve fibers; histologic sections; axoarchitectonic; cytoarchitectonic; cerebral cortex; immunohistochemistry; neuroimaging; mapping; videomicroscopy; image analysis; traverses; excess mass

ABSTRACT The field of quantitative analysis and subsequent mapping of the cerebral cortex has developed rapidly. New powerful tools have been applied to investigate large regions of complex folded gyrencephalic cortices in order to detect structural transition regions that might partition different cortical fields of disjunct neuronal functions. We have developed a new mapping approach based on axoarchitectonics, a method of cortical visualization that previously has been used only indirectly with regard to myeloarchitectonics. Myeloarchitectonic visualization has the disadvantage of producing strong agglomerative effects of closely neighbored nerve fibers. Therefore, single and neurofunctional-relevant parameters such as axonal branchings, axon areas, and axon numbers have not been determinable with satisfying precision. As a result, different staining techniques had to be explored in order to achieve a suitable histologic staining for axon visualization. The best results were obtained after modifying the Naoumenko-Feigin staining for axons. From these contrast-rich stained histologic sections, videomicroscopic digital image tiles were generated and analyzed using a new fiber analysis framework. Finally, the analysis of histologic images provided topologic ordered parameters of axons that were transferred into parameter maps. The axon parameter maps were analyzed further via a recently developed traverse generating algorithm that calculated test lines oriented perpendicular to the cortical surface and white matter border. The gray value coded parameters of the parameter maps were then transferred into profile arrays. These profile arrays were statistically analyzed by a reliable excess mass approach we recently developed. We found that specific axonal parameters are preferentially distributed throughout granular and agranular types of cortex. Furthermore, our new procedure detected transition regions originally defined by changes of cytoarchitectonic layering. Statistically significant inhomogeneities of the distribution of certain axon quantities were shown to indicate a subparcellation of areas 4 and 6. The quantification techniques established here for the analysis of spatial axon distributions within larger regions of the cerebral cortex are suitable to detect inhomogeneities of laminar axon patterns. Hence, these techniques can be recommended for systematic and observer-supported cortical area mapping and parcellation studies. *Microsc. Res. Tech. 63:220–243, 2004.* © 2004 Wiley-Liss, Inc.

INTRODUCTION

One of the most extensive studies of the myeloarchitectonic structure of the human cerebral cortex has been provided by Vogt (1911) and Vogt and Vogt (1919). On the basis of comparative observations, these researchers characterized more than 200 different cortical areas in 40-μm thick sections of whole human brains stained with a Kultschitzky-Pal modification of the Weigert-myelin method. But this strongly supported subdivision of the cortex has been criticized in subsequent published reports (Lashley and Clark, 1946; Bailey and von Bonin, 1951; Le Gros Clark, 1952; Sholl, 1956). Recently, finer parcellations of the cortex have been described (Zilles et al., 1991a; Zilles and Palomero-Gallagher 1999) and new in vivo imaging evidence has been offered (Geyer et al., 1996; Zilles et al., 1996) regarding the structural subregions of the human cerebral cortex.

In myelin-stained sections, Cécile and Oskar Vogt (Vogt and Vogt, 1919) defined their "myeloarchitectonic basic scheme" ("myeloarchitektonisches Grundschema") of two types of nerve fibers: thin basic fibers and thick singular fibers. The distribution of nerve fibers exhibited a typical pattern of layers, e.g., the

Contract grant sponsors: Peter Dornier, Gerhard Ten Doornkaat Koolman, and the Possehl Foundation.

*Correspondence to: Oliver Schmitt, Institute of Anatomy, University of Rostock, Gertruden Str. 9, D-18055 Rostock, Germany.
E-mail: schmitt@med.uni-rostock.de

Received 23 October 2003; accepted in revised form 26 December 2003
DOI 10.1002/jemt.20033
Published online in Wiley InterScience (www.interscience.wiley.com).

© 2004 WILEY-LISS, INC.

TABLE 1. Myeloarchitectonic and cytoarchitectonic layering of the isocortex of man[1]

Cytoarchitectonic		Myeloarchitectonic				
		Numbering				
Roman numeral	Term of layer	Vogt	Batsch	Term of layer		Eponym
I	Lamina molecularis (plexiformis)	1o	1^1	Sublamina superficialis	Lamina tangentialis	Stria Exner
		1a	1^2	Pars externa sublaminae intermediae		
		1b	1^3	Pars interna sublaminae intermediae	Stria laminae molecularis	
		1c	1^4	Sublamina profunda		
II	Lamina granularis externa (corpuscularis)	2	2	Stria laminae granularis externa Lamina dysfibrosa		Stria Kaes-Bechterew
III	Lamina pyramidalis externa	3^1	3^1	Lamina superficialis	Lamina suprastriata	Stria Kaes-Bechterew
		3^2	3^2	Sublamina intermedia		
		3^3	3^3	Sublamina profunda		
IV	Lamina granularis interna	4	4	Stria laminae granularis interna		Stria Baillarger externa
V	Lamina pyramidalis interna (ganglionaris)	5a	5^1	Lamina interstriata superficialis	Lamina intrastriata Stria laminae pyramidalis interna	Stria Baillarger interna
		5b	5^2	Stria Baillargeri interna		
VI	Lamina multiformis	6aα	6^1	Lamina substriata	Lamina infrastriata (substriata)	Stria Kaes
		6aβ	6^2	Lamina limitans externa		
		6bα	7^1	Lamina limitans interna		
		6bβ	7^2	Zona corticalis albi gyrorum		

[1]The subdivision of the myelin stained cortex by Vogt is based on the publication Vogt and Vogt (1919) and Batsch (1956). This scheme was illustrated by Hellwig (1993), Zilles and Palomero-Gallagher (1999).

"myeloarchitectonic basic scheme" (Vogt and Vogt, 1919) divided by "laminae myeloarchitectonicae" (Table 1) that can change in varying degrees between different areas. Such changes of the myeloarchitectonic basic scheme may be indicators of transition regions of adjacent cortical areas. Furthermore, nerve fiber courses (e.g., those involving radial, oblique, or horizontal fibers) must be taken into consideration to differentiate myeloarchitectonics (Hellwig, 1993).

However, specific information about and differentiation among efferents leaving a certain cortical area such as intracortical fibers (i.e., Martinotti cells), horizontal collaterals, and afferent inputs can be obtained only through Golgi impregnations or tracing techniques (Frotscher, 1992). In this study, such features of functional types of axonal projections could not be investigated.

The distribution and density of nerve fibers (axons, neurites) tend to show a commonly accepted layering, as summarized in Table 1. Certain patterns of myelin distribution have been differentiated by visual inspection (Vogt, 1911; Vogt and Vogt, 1919; Hopf, 1968a). In principle, based on these studies, six different patterns—unistriate, propreunistriate, bistriate, unitostriate, propeastriate, astriate—can be observed in the frontal lobe of the human brain, each basically differentiated by the respective extension of the inner (located within lamina Vb) and outer (located within lamina IV) stripe of Baillarger (Baillarger, 1840). Use of these stripes of Baillarger has been widely accepted for determination of cortical parcellation, since they exhibit areal variations that are visible at low magnifications, often by the unaided eye. Hopf (1966, 1968a,b) developed a photometric method to quantify the extent of myelination in the cerebral cortex and to objectively compare the different patterns of myelin occurrence of different areas in the parietal (Hopf, 1969; Hopf, 1970) and temporal lobes (Hopf, 1966).

Most studies have quantified the distribution of the myelin sheets in the cerebral cortex at a microscopic scale (Braitenberg, 1962; Hopf, 1969, 1970; Hamano, 1996) or fiber tracts at a macroscopic scale (Bürgel et al., 1999; Rademacher et al., 1999) are quantified or mapped. Other investigations have focused on analyzing the spatial dendritic structures (Burke and Marks, 2002; van Oyen and van Pelt, 2002) at the microscopic scale to obtain data for modeling artificial neurons (Ascoli et al., 2001).

The quantitative analysis of nerve fibers in histologic sections can be performed by identifying single fibers (high resolution) and characterizing them by measuring certain structural features, or with a mediocre resolution, by quantifying the distribution of gray values or imaged staining intensities of nerve fibers within the cerebral cortex or subcortical regions (Rademacher et al., 1999). Using the latter approach, quantitative myeloarchitectonics seems to offer information that is complementary only to cytoarchitectonics. Furthermore, myeloarchitectonic studies provide evidence for a higher degree of parcellation of certain cortical regions (Vogt, 1911; Strasburger, 1937; Gerhardt, 1940; Batsch, 1956) which were confirmed and elaborated further by receptor architectonic investigations (Zilles, 1991a,b, 1995, 1996; Geyer et al., 1998; Zilles and Palomero-Gallagher, 1999).

Perikaryon stains such as Nissl or Gallyas stains usually coincide with changes in the distribution pattern of intracortical myelinated fibers (Hellwig, 1993). Additionally, Strasburger (1937) and Sanides (1962) investigated the human frontal lobe alternately stained by the Nissl and the Heidenhain-Woelke methods. They observed that the inner and outer stripes of Baillarger disappear in a dense net of fibers between layer III and the white matter border. This change of the distribution of axons can be explained by the morphology and distribution of pyramidal cells in layers III

to VI, since giant pyramidal cells of Betz have a relatively small density and are distributed between layer V and the homogeneous white matter border. Thus, these studies indicate that the myeloarchitecture coincides with the distribution and the projection area of neurons. This relationships were investigated extensively by Hellwig (1993) using the structural relation of myelo-cytoarchitectonics to derive myeloarchitectonic models from cytoarchitectonic data.

So far, however, information about nerve fiber lengths, amounts, branching variations, and their orientations have not been taken into consideration. Quantitative information derived from larger optical resolutions is important to ascertain spatial changes of specific architectonic components of nerve fibers. This information cannot be obtained by myeloarchitectonic staining alone since the adjacent myelin sheets are agglomerated and single axons can no longer be differentiated. Also, tracking of nerve fibers in myelin stainings is not possible because points of bifurcation are always unmyelinated (Ramon y Cajal, 1911; Chang, 1952).

Therefore, a histologic procedure must be determined that produces sharp and contrast-rich stained nerve fibers. This is a prerequisite for quantifying nerve fibers by image analytical methods. It is probable that parameters of axoarchitectonics extracted by such a procedure may relate directly to functional changes within the cerebral cortex. Furthermore, mappings of these specific parameters can help to identify transition regions that may correspond to changes in functional representations (Amunts et al., 1995, 1998, 1999; Geyer et al., 1996, 1997, 1999; Schmitt et al., 2003).

Nevertheless, the image analysis-based quantification of nerve fibers in histologic sections presents three major problems:

1) The spatial fiber distribution or geometry is complex, which means that fibers may follow abrupt changes or slightly twisted courses combined with multiple bifurcations.
2) This complex fiber-geometry has to be analyzed in 2D-projections instead of 3D-image-stacks derived from the histologic section space, because the mass of data obtained by 3D evaluations currently cannot be handled properly.
3) The most efficient and specific visualizations of nerve fibers by histologic stainings make use of silver nitrate, a procedure that often leads to inhomogeneous staining results and artifacts that will cause serious problems for automatic image analysis.

For this reason, a robust image analysis algorithm had to be developed in order to reliably quantify larger areas of the cerebral cortex stained for nerve fibers and to map the determined quantities in relation to their corresponding spatial locations.

The objective of this study is multifold: 1) to present a reliable staining method for nerve fibers; 2) to offer a robust image analytical procedure for evaluating nerve fibers in histologic sections; 3) to introduce mappings of suitable nerve fiber quantities; 4) to statistically evaluate such parameter maps for transition region detection; and 5) to obtain some additional information on the wiring scheme of certain parts of the human cerebral cortex.

MATERIALS AND METHODS

Histologic Methods

The brains of two female donors age 81 (SNR217) and 77 (SNR334) (body donor program of the Institute of Anatomy of the University of Lübeck) exhibiting no neuropathologic changes were fixed 6 hours postmortem in Somogyi's fixative (Somogyi and Takagi, 1982) by immersion for 3 months. Thereafter, the agranular transition region of area 4 and area 6 (SNR217) and the granular somatosensory area 3 (SNR334) were prepared macroscopically and embedded in paraffin wax (Paraplast Plus, VWR no. 631N1272). Further blocks of tissue of the transition region area 4 to area 6 of brain SNR217 were processed for immunohistochemistry. Twenty-micrometer-thick histologic sections were cut with a sliding microtome. These sections where stained using different fiber staining protocols (Figs. 5, 6):

- Benda-Spielmeyer: Romeis (1989)
- Klüver-Barera: Romeis (1989)
- Kultschitzky: Romeis (1989)
- Weigert-Pal: Romeis (1989)
- Naoumenko-Feigin: Naoumenko and Feigin (1967)
- Loyer: Loyez (1910); Ráliš et al. (1973)
- Schroeder-Braak: Braak (1980)

The method of Naoumenko and Feigin (1967) was favored because it provides images that are rich in contrast while preserving fine details. The sections were stained after optimizing the procedure for visualizing nerve fibers (axons, neurites). In brief, the staining solution consisted of a pH 7.6 borax buffer (85 ml 0.2M boric acid: 14.49 g boric acid + 1,000 ml distilled water, 15 ml 0.05M borax: 19 g borax + 1,000 ml distilled water, 10 ml 0.1% NaCl, 1,000 ml distilled water). The final staining solution consisted of 100 ml of borax buffer and 3 ml 0.1% silver nitrate. Paraffin sections were deparaffined and washed in distilled water for 5 minutes. These sections were impregnated in the staining solution at 56°C for 18–24 hours in the dark, directly followed by the reduction solution (1 g hydroquinone + 2 g sodium sulfite + 95 ml distilled water) at 30–37°C for 5 minutes. The sections were then washed (2× distilled water 1 min each). The development was performed in a 1% gold chloride solution ($AuCl_3 \times HCl \times 3H_2O$) at room temperature (RT) (20–37°C) for 5–10 minutes, followed by two washes in distilled water (each 1 minute), 2% oxalic acid (RT) for 4–10 minutes, fixation in 5% sodium thiosulfate (RT) for 3 minutes, and finally two washes of distilled water. The sections were then dehydrated and mounted in Entellan (Merck, Darmstadt, Germany; 1.07961).

A third brain from a 48-year-old female (body donor program of the Institute of Anatomy of the University of Lübeck) without neuropathologic or psychiatric disorders was removed from the cranium and fixed by immersion in an isotone neutral buffered 4% paraformaldehyde fixative. After 48 hours the regions of interest (prefrontal gyrus, precentral sulcus, postcentral gyrus) were prepared (Fig. 1) and fixed for an additional 48 hours. Serial sectioning was performed using a vi-

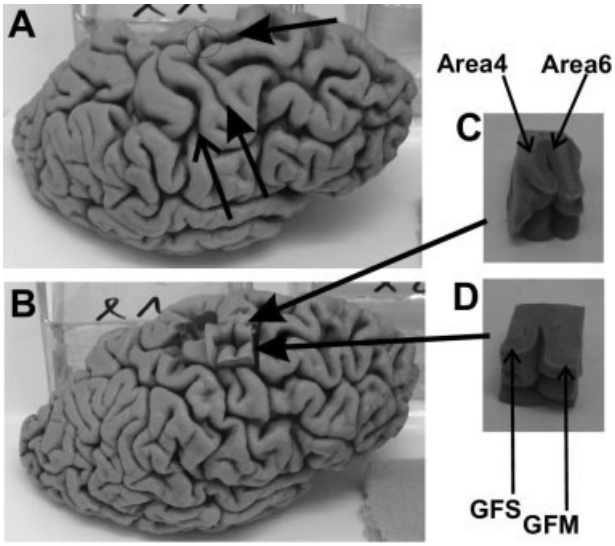

Fig. 1. Each specimen **A** is photographed from different perspectives (**C, D**) to provide evidence for the macroscopic location of the specimens that were analyzed. Notice the complex T-shaped geometry **B** of this specific cortex region where the superior frontal gyrus meets the precentral gyrus. To evaluate such regions by serial sectioning and image analysis leads to complex problems. The lower filled arrowhead points to the precentral gyrus, the upper filled arrowhead points to the superior frontal sulcus and the open arrowhead to the central sulcus. GFS, superior frontal gyrus; GFM, medial frontal gyrus.

bratome (VT 1000S, Leica). The section thickness was 50 μm. Sections were immunohistochemically processed in a free-floating state. A primary antibody against acetylcholinesterase (Biotrend 9-0030-2229), among others not shown here, was applied. The visualization of the antibodies was amplified by using tyramide.

The sections were rinsed three times at 20-minute intervals in 0.1M phosphate-buffered saline (PBS, pH 7.4; 4× PBS-solution: 45 g NaCl + 1.352 g NaH_2PO_4 H_2O + 14.397 g Na_2HPO_4 12 H_2O + 1000 ml H_2O distilled water). The endogen peroxidase was blocked by 3% H_2O_2 for 10 minutes followed by further rinsing in PBS. Endogenous avidin and biotin binding sites were blocked with biotin blocking solution (Dako, Carpinteria, CA; X0590), containing 0.1% avidin and 0.01% biotin in 0.05M Tris-HCl, pH 7.2–7.6. Nonspecific protein binding was blocked for 15 minutes with a protein blocking solution (Dako X0909).

Biotinylated tyramine was mixed according to Adams (1992), that is, 100 mg HNS-LC-Biotin (sulfosuccinimidyl-6-biotinimide hexanoate) (Toronto Research Chemicals, Toronto, Canada; s69025) and 31.2 mg tyramine-HCl (Sigma, St. Louis, MO; T-2879) were mixed in 40 ml of 50 mM borax buffer (pH 8). After 12 hours at room temperature (20°C) the solution was filtered through a 0.45-μm pore filter. The resulting concentration of biotinylated tyramine (BT) was ~7 μM. This solution can be used for up to 6 months when stored at 4°C or for long-term storage at –20°C for 2 years (tested here). Freezing and thawing does not negatively affect the solution. Before use, 1 μl of the 7 μM solution and 1 μl 30% H_2O_2 were diluted in 1 ml 0.1 M PBS. The Dako protein-blocking solution reduces the background more than any other tested blocking solution (normal goat serum, dry-milk solution, or bovine albumin solution). The biotinylated secondary antibody against mouse was produced in goat (Dako E0433, if the primary antibody is polyclonal a secondary antibody against rabbit from Dako K1498 can be used) and diluted 1:500 in 0.1% bovine serum albumin, 10% normal goat serum, and 0.05% thimerosal in PBS (pH 7.4). The streptavidin-biotin-complex conjugated with HRP (Dako K0377) was produced 30 minutes before incubation by mixing 8 μl streptavidin and 8 μl HRP conjugated biotin each in 1,000 μl PBS. The HRP-conjugated streptavidin (Dianova 016-030-084) was used in a concentration of 1:200 in PBS.

Image Acquisition

The mounted sections were fixed on an xy-motorized stage of a light microscope (Universalforschungsmikroskop, Zeiss). A rectangular region of interest (ROI) was defined interactively at low resolution (objective 2.5×, optovar 1.25×). A computer program was interpreted by the IBAS 2.5 system (Zeiss Vision) and shifted the section automatically in a meandering fashion through the ROI at a resolution of 0.503 × 0.503 μm^2/ pixel edge length (objective 25×, optovar 1.25×). On the screen the images appeared with a size of 170 × 170 mm^2. After each shift the plane of focus was adjusted by determining the maximum of the gray intensity variance of a sample of optical planes above and below the actual plane of focus. These images were corrected for illumination inhomogeneities such as shading which results from long scanning duration of larger ROIs and slight fluctuations in the microscope illumination device can lead to slight shading effects.

After each shift, the field of view was recorded as an 8-bit gray-level image of 512 × 512 pixels. The image-tiles were transferred to an Intel PC running with Linux 7.3 and a downsampled (×0.125) image-mosaic was computed to get an overview of the digitized ROI and to verify the quality of the scan visually.

Image Analysis

The purpose of the algorithm was to provide information about the spatial distribution of nerve fibers at different levels of abstraction. The processing chain is shown in Figure 2. Initially, nerve fibers were enhanced and other structures (e.g., cell nuclei) were suppressed. We observed that applying the Sobel edge operator leads to unsatisfying enhancements. The results obtained by the closing top-hat transformation exactly enhances the structures of interest that must be separated. The top-hat transformation is a combination of certain basic morphologic operators defined

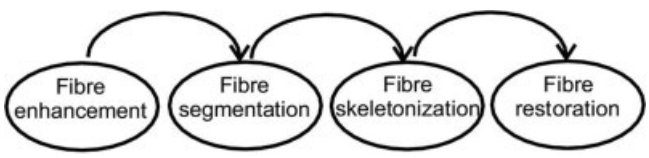

Fig. 2. The main steps of the image analytical approach developed for fiber analysis.

below (for further details, see Giardina and Dougherty, 1988; Dougherty, 1993; Serra and Soille, 1994).

The enhancement procedure was followed by segmentation of the nerve fibers in order to obtain a binary image. Global thresholding or a shifting threshold method provides unsatisfying results. With a modification of the Otsu-threshold method (Otsu, 1979) we obtained optimal segmentation results primarily independent of staining or illumination fluctuations (APPENDIX 2: Segmentation).

Skeletonization and Restoration

The skeletons, here the morphological endoskeletons, of the segmented bilevel images were determined with the four subcycle algorithm (Tamura, 1978; Arcelli et al., 1980; Zamperoni, 1979) using eight masks (Zamperoni, 1979) until binary objects are ultimately thinned. Here, we do not differentiate between thinning, medial axes transform, or skeletonization as done by Ji and Piper (1992). The resulting skeleton image must be restored in order to remove biologically impossible (cycles, star shapes) nerve fiber courses that are caused by 2D-projections of 3D-distributed objects. However, due to loss of the 3D-information of nerve fiber courses an exact restoration can be approximated only. Cycles were removed after detecting them by flood filling (Foley, 2000) and opening one or all (can be defined by the user) crossings or branches joining the cycle (Fig. 3e). Furthermore, short skeletons are filtered out (Fig. 3d,e). A nerve fiber that travels through the section space may appear at the upper side, then change its direction to the lower side and again ascend. In 2D-projection some parts of the same fiber will be missing. The missing segment can be reconstructed by applying the Hough-transform that connects linear line segments (Zamperoni, 1979). Since nerve fibers have extremely short nonlinear courses, very many segments would have to be reconstructed. This approach would be time-consuming. Therefore, an alternative algorithm was implemented that elongates fiber endings only if their distances will be reduced.

Distanglement

A problem occurring with quantification concerns determining which fiber segments belong to a certain fiber, since fibers can cross and branch in 3D and we are limited to analyzing the 2D-projection of the 3D-fiber distribution. Therefore, three different types of fiber rearrangement procedures were implemented in order to approximate the real anatomy and to apply different distanglement schemes for different situations of fiber-distributions or architectonics (Fig. 3f). The following procedures were implemented:

1. No separation of connected fibers.
2. Maximal separation: All crossings are removed.
3. Minimal separation: After removing cycles and lines without branchings and crossings remaining crossings were split. The connection or fiber that lies in front of the largest angle of the crossing is removed because these fibers are the least likely to belong to a natural biological course of nerve fibers.

Parameters and Quantification

The number of fibers, branchings, mean length, fractal dimension, or roughness were determined by analyzing the distangled images, the mean area of fibers were calculated from the segmented images, and the mean intensity as well as mean variance from the original image tile by masking it with the segmented image.

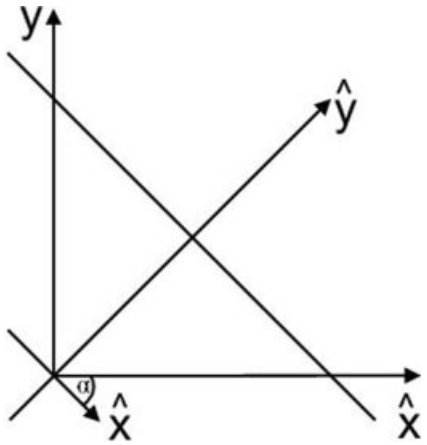

Fig. 3. Coordinate transformation.

The orientation, of the fibers is calculated in skeletonized fiber images where $P_1 = (x_1,y_1)$ and $P_2 = (x_2,y_2)$ define a line segment. The angle α was calculated as usual by:

$$\alpha = 90° - \left(\arctan\left(\frac{y_2 - y_1}{x_2 - x_1}\right)\frac{180°}{\pi}\right).$$

In order to receive positive angles only P_1 and P_2 have to be chosen such that $x_1 < x_2$ and $y_1 < y_2$. In case $x_1 = x_2$, that is, P_1 and P_2 are lying underneath each other, α is set to 90° (right angle).

To overcome problems caused by convex and concave courses of skeletonized nerve fibers having the same orientation angle but which are mirrored (e.g., 45° left side vs. 45° right side oriented fibers) we decided to implement a tensor-based procedure for measuring orientation of nerve fibers (Bigün and Granlund, 1987). Opposite orientations of a nerve fiber are averaged to one orientation by this procedure. One major advantage of the tensor method is the determination of an unambiguous orientation, more than one orientations, or no orientations. Another advantage of the tensor-based procedure is that it provides additional information on the reliability of fiber orientation estimates. Therefore, it can be determined whether the computed angle represents the actual orientation, or if it is merely the result of averaging over a number of different orientations. The tensor algorithm can be applied to different images. We observed that using the top-hat-transformed images with low-pass-filter size of 5×5 pixels produces similar results as using skeleton or bilevel segmented images. In APPENDIX 3, a short introduction to the tensor method is given (see also Fig. 3). The physical analog to the tensor used here is the inertia tensor. For further details, refer to APPENDIX 3: Orientation.

The roughness of nerve fibers was computed by determining the fractal dimension applying the box-counting method (Landini and Rippin, 1996; Ristanović et al., 2002). The tracings of nerve fibers were covered with gratings of increasing sizes and the number of intersecting squares (boxes) with the fiber were counted. Since the fibers are skeletonized the borders were quantified only. For each pixel $f(x,y)$ ($\forall x, y \in \mathbf{N}$: $0 \leq x, y \leq 512$) in a frame of increasing size ϵ the number of connected pixels $M(\varepsilon)$ were counted. The fractal dimension α is calculated by relating the number of pixels and the frame size:

$$\alpha = -\frac{\log(M(\varepsilon))}{\mathrm{Log}(\varepsilon)}.$$

The framesize ε will be stepwise enlarged until $M(\varepsilon)$ stays constant. Then all results for α are averaged.

If the frame is completely filled, then we get $\alpha = 2$. A straight line (one-dimensional) leads to $\alpha = 1$. Because the fractal dimension is calculated for skeletons, it is impossible that α becomes 2. However, it is possible that α gets smaller than 1, because a skeleton may end in a frame.

The results of computing the fractal dimension are transformed into an 8-bit gray level image. Therefore, α is adapted by the following relation:

$$\alpha_m = 100 \cdot (\alpha + 1).$$

At least the variance and mean of the gray intensities of the nerve fibers are determined by masking the original gray level image with the segmented bilevel image. These parameters offer information about the staining intensity and the homogeneity of the histologic nerve fiber visualization.

Since image compositions (image mosaic) consist of image tiles that are analyzed by image analytic procedures, separate information is missing at the border of an image tile. Adding this information from the adjacent image would not solve this problem, since the same effect will occur at the new borders of an image that is composed of its adjacent images.

This missing information at the image borders produces block effects by certain image-processing functions. The top-hat-transformation is calculated for a single pixel by considering the maximal and minimal intensities of its surrounding. At the image border the surrounding of a pixel consists of fewer pixels, leading to an approximation of the top-hat-function here. The threshold of adjacent images may differ and, therefore, fibers that are passing the image borders could be binarized insufficiently. This means that the same nerve fiber will be segmented in one image but not in the adjacent. The skeleton algorithm fulfils the criteria of:

1. Curve thickness property (skeleton consists of a width of single image points);
2. Topology preserving property (topological connectedness relation of skeleton and original image are the same);
3. Medial axis property (skeleton curve lies in the middle to its affiliated object);
4. Noise robustness property (thick or rugged objects should not lead to too many irrelevant mini skeleton branches); and
5. Convergence property (skeletonization should converge to a stable minimal skeleton after a certain subcycles of operations were achieved).

However, the algorithm operates from a point outside the image inwardly to the image inside, leading to a shift of the skeleton of those thinned nerve fibers that are passing the image borders and therefore to a more or less strong concentration of skeleton pixels in the center of the image. To reduce these block effects each border of an image was mirrored by an 88-pixel-wide border as shown in Figure 4.

Traversing and Analyzing the Parameter Maps

The parameters described above are mapped to parameter maps (Figs. 8–10, 12). Each parameter map can be described only. However, we are interested in quantitative changes of the lamination pattern of the parameters presenting structural transition zones within the cerebral cortex that may indicate functional changes, too. Therefore, after analyzing an original image tile of the image mosaic each parameter was written to its corresponding location in the parameter map. In these maps the cerebral cortex was outlined by an outer and an inner contour line as described by Schmitt and Böhme (2002). Then, perpendicular to the cortical surface traverses were calculated applying an electrodynamic model (Schmitt and Böhme, 2002) and the parameters under the traverse were read out and written into a profile array. That means that each cortex segment within the parameter maps can be scanned by this method.

Finally, we want to know if statistically significant changes can be observed within the course of the cerebral cortex respectively within the profile array. This was done by excess mass analysis (Müller and Sawitzki, 1991; Schmitt et al., 2003) and statistical testing of excess mass differences by the multiple linear rank test (Dümbgen, 2002).

Statistically significant changes (jumps) are documented in upward (increase of layering) and downward (decrease of layering) jump diagrams. These diagrams indicate those locations within the profile arrays—and therefore locations within the original course of the scanned cerebral cortex too—where the linear rank test has detected structural changes at a significance level of $P \leq 0.01$.

RESULTS

Nerve Fiber Visualization

Eight different staining protocols were applied to determine which method offers optimal results and provides suitable contrast as well as details sufficient for further image analytic evaluations. Low-resolution overviews (Figs. 5, 6) are presented beside high-resolution (660×) images. The myelin methods (Benda-Spielmeyer, Klüver-Barera, Kultschitzky, Weigert-Pal, Weil [Romeis (1989)], Loyer, Schroeder-Braak) produces very different staining results. The Schroeder-Braak (Braak, 1980) method was favored since it is not necessary to precondition the tissue as in the Weigert-Pal method. In Figure 6c, a section of the frontal gyrus

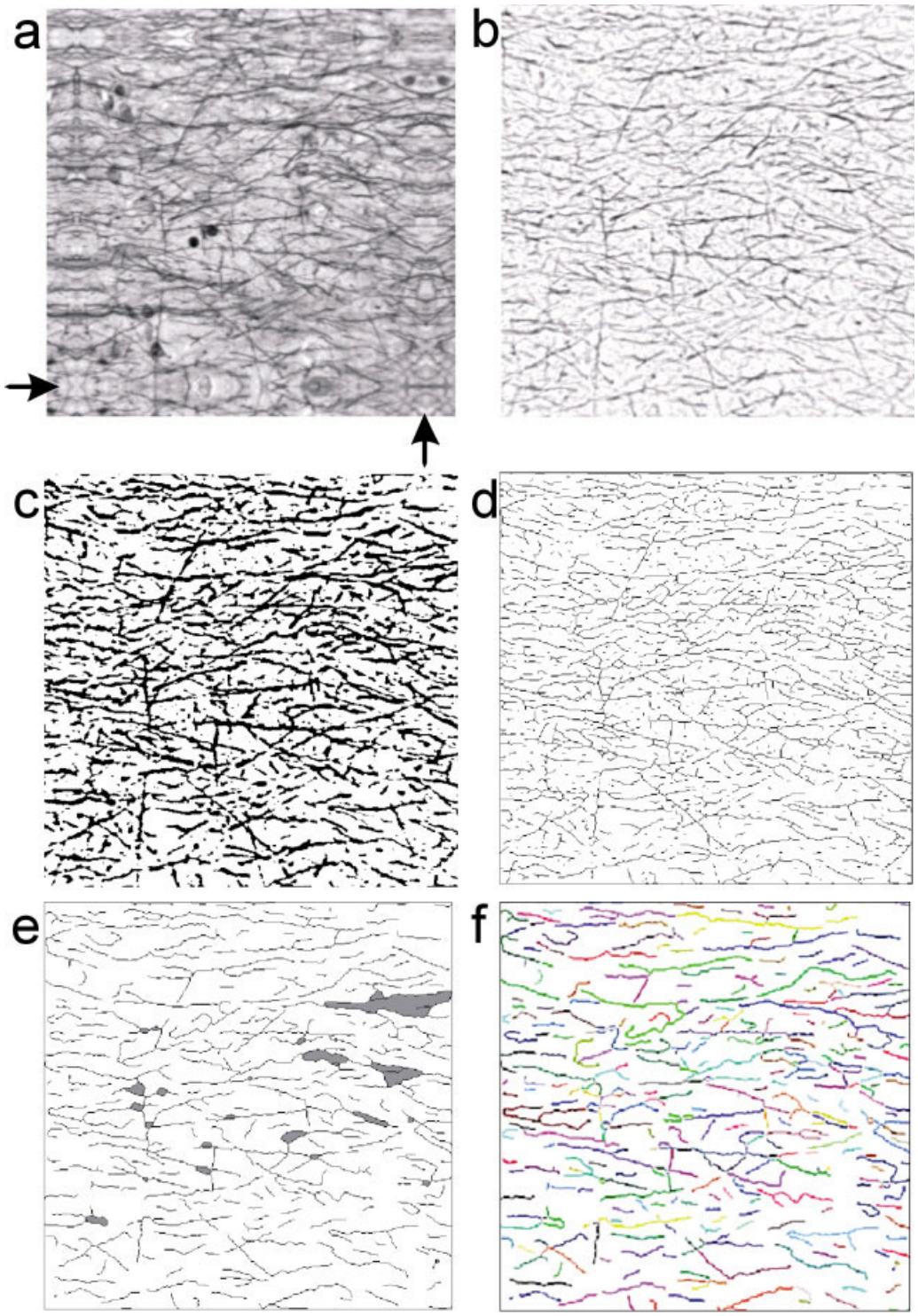

Fig. 4. The four major image analytical steps are documented here. **a:** An original histologic image stained for nerve fibers according to Naoumenko-Feigin. The borders of the 512 × 512 pixel (0.503 μm / pixel edge length) large image are mirrored by a width of 88 pixels (arrows). Finer details of the dark and contrast rich stained axons are visible. Some axons elapse out of the plane of focus, yielding problems within the digital restoration and distanglement. This image tile is contained in the image mosaic of area 3 shown in Figure 7g. **b:** Fibers are enhanced by applying the top-hat transform. **c:** The conditional Otsu-segmentation provides a bilevel image containing sufficient and relevant foreground information. **d:** The binary image is skeletonized as described in the text. Small pixel accumulations are filtered followed by opening cyclic structures that are detected by (**e**) flood filling. **f:** Larger fiber complexes are distangled by the restoration algorithm. Single fibers are displayed by different colors. [Color figure can be viewed in the online issue, which is available at www.interscience.wiley.com.]

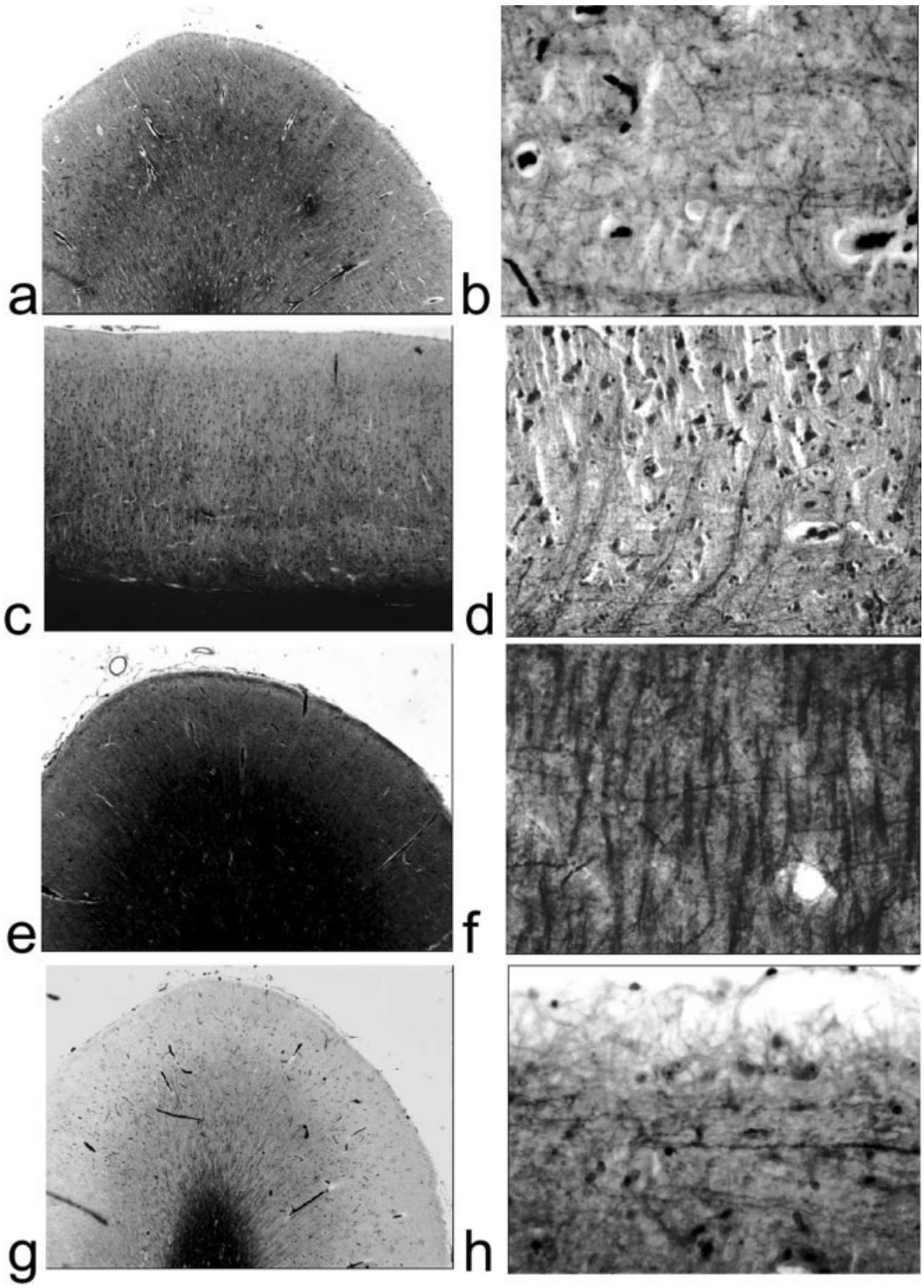

Fig. 5. Here we show the histologic myelin and axon stainings which provided the best results. The macroscopic view is shown on the left side with a frame that is enlarged on the right side to show microscopic details. **a:** Naoumenko-Feigin, 20×. **b:** Naoumenko-Feigin, 660×. **c:** Schroeder-Braak, 20×. **d:** Schroeder-Braak, 660×. **e:** Weigert-Pal, 20×. **f:** Weigert-Pal, 660×. **g:** Weil, 20×. **h:** Weil, 660×.

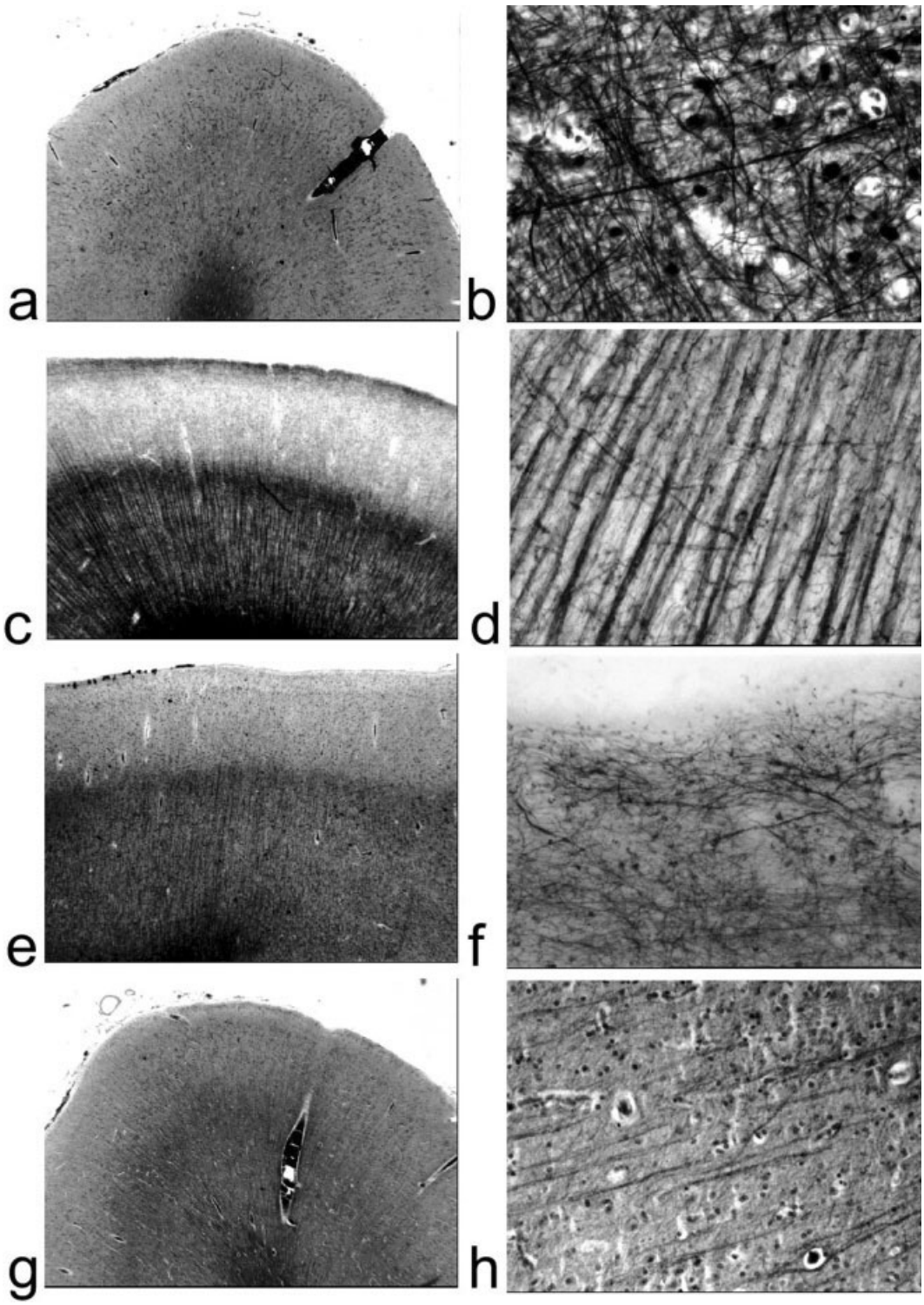

Fig. 6. Here the histologic myelin and axon stainings which provided the best results are continued. On the left side the macroscopic view is shown with a frame that is enlarged on the right side to show microscopic details. **a:** Benda-Spielmeyer, 20×. **b:** Benda-Spielmeyer, 660×. **c:** Klüver-Barrera, 20×. **d:** Klüver-Barrera, 660×. **e:** Kultschitzky, 20×. **f:** Kultschitzky, 660×. **g:** Loyez, 20×. **h:** Loyez, 660×.

clearly showing the outer horizontal stripe in layer 4 is presented; no demarcation of the inner horizontal stripe can be seen. Therefore, area 6 located here belongs to the unistriate type of cerebral cortex. The higher magnification of this staining (Fig. 6d) shows agglomerates of multiple myelin-sheets as well as smaller horizontal and oblique myelin sheets within layer VI.

The modified method of Naoumenko and Feigin (1967) leads to sharp and contrast-rich nerve fiber stainings suitable for image analytical quantification (Fig. 6b). Using a magnification of 660×, single nerve fiber diameters are presented by several pixels, providing enough information for reliable fiber enhancement and segmentation.

Traversing the Image Mosaics for Cyto- and Axoarchitectonics

In the following sections, the results from the original image mosaic of cytoarchitectonics from area 4 and area 6 are described (Fig. 7) before the original image mosaics of the axoarchitectonic are characterized by averaged profile curves. The results yielded by traversing the axoarchitectonic parameter maps will be presented in the following subsections.

Cytoarchitectonic Pattern of Areas 4 and 6. The cytoarchitectonic pattern of areas 4 and 6 was quantified in order to define layer borders in an adjacent histologic section of the same brain, resolution, and traverse generating parameters (Fig. 7a). Area 4 (Fig. 7c) is characterized by a small subpeak in layer I followed by a relatively continuous increase of cell density with a global peak in layer III. Then we observed a decrease of cell density with a local subpeak just above layer V. From layer V to layer VI the cell density decreases strongly.

The cytoarchitectonic pattern of area 6 (Fig. 7b) shows some major differences in comparison to area 4. The increase of cell density in layers I and II is stronger than in area 4. Two large subpeaks are typical in area 6 for layer III and a profile-plateau from layer III to layer V with a smaller subpeak. Then a very strong decrease of cell density within layer V, a small subpeak in layer VI, and a further decrease to the white matter border are visible.

Axon Distribution Pattern in Area 4. The image mosaic of the Naoumenko-Feigin-stained histologic section containing area 4 and area 6 was scanned by the traverse generating method in the same section (Fig. 7d). The averaged profile, consisting of 1,600 single profiles, is shown in Figure 7f. Layer I shows a low density of axons which strongly increases within layer II. The relative increase of axon concentration in layer III is weaker than in layer II. In layer V and VI the increase of axons becomes larger than in layer III. The small layer V of this axoarchitectonic profile is comparable with the internal stripe of Baillarger of myeloarchitectonics.

Axon Distribution Pattern in Area 6. Rostral to the precentral gyrus a part of area 6 is delineated (Fig. 7d). In principle, the distribution pattern of axons in area 6 is comparable to the pattern found in area 4. However, layer II shows a small local peak and nearly no increase in the amount of axons in comparison to layer II of area 4 (Fig. 7e). Furthermore, a small initial subpeak in layer III was found. In layer III the increase of axons is stronger than in area 4. Layer V appears to be smaller (the small subpeak of the axoarchitectonic profile is comparable with the internal stripe of Baillarger of myeloarchitectonics) and the increase of axons within layer VI is stronger than in area 4.

Axon Distribution Pattern in Area 3. The axon distribution pattern in area 3 (Fig. 7g) shows a pronounced local minimum of axons in layer I and a rapid increase with a pronounced subpeak in layer II (Fig. 7h). A further weak subpeak within an increase of axons indicates the relatively small layer III. In layer IV a strong increase with smaller subpeaks indicating sublayers of layer IV were detected. The large peak of layer IV of the axoarchitectonic profile is comparable to the external stripe of Baillarger in myeloarchitectonic preparations. Layer V can be characterized by a small subpeak (comparable to myeloarchitectonic internal stripe of Baillarger) and a succeeding increase until layer VI. The latter contains a wider subpeak and a final decrease up to the white matter border.

In comparison to the agranular motoric areas 4 and 6, the upper layers of area 3 are more pronounced and an increase in axon concentration within layers V and VI can be observed.

Quantitative Axoarchitectonics

The parameters described in Materials and Methods were quantified in two different image mosaics of histologic sections (Figs. 8, 10) stained with the Naoumenko-Feigin method. In order to show differences of fiber architectonics found by quantification and visualization in parameter maps of granular and agranular regions of the cerebral cortex area 3 (Fig. 10) and the transition region of area 6 (Fig. 9) to 4 (Fig. 8) are analyzed.

The mosaic shown in Figure 10 (SNR334) consists of 27 × 11 image tiles (area 3) and the mosaic in Figure 8 (SNR217) of 44 × 42 tiles containing areas 6 and 4. All image tiles have a size of 512 × 512 pixels. The parameter maps for these examples are shown in Figures 8–10.

Morphometric and Densitometric Axon Parameters of Area 4. The morphometric and densitometric parameters were determined in each image tile and mapped in a parameter map. Therefore, eight parameter maps were calculated (Fig. 8). Block effects were filtered with a Gauss-filter. The filtered parameter maps were traversed within the same region of the section as described before. The mean profiles are summarized in Figure 8. We observed that the profiles of the area, number, length, nodes, and roughness have similar courses. Therefore, they were averaged and summarized in one morphometric parameter map (Fig. 8).

This profile shows a peak within layer I and a local minimum within layer II. A smaller initial peak at the beginning of layer III and a global peak within layer III was found. The profile displays a slight subpeak within layers V and VI above the white matter border.

The distribution of angles have to be considered separately, since their distribution exhibits a completely different course. Large angles or perpendicular orientations of nerve fibers to the cortical surface are presented by small normalized values in the diagram.

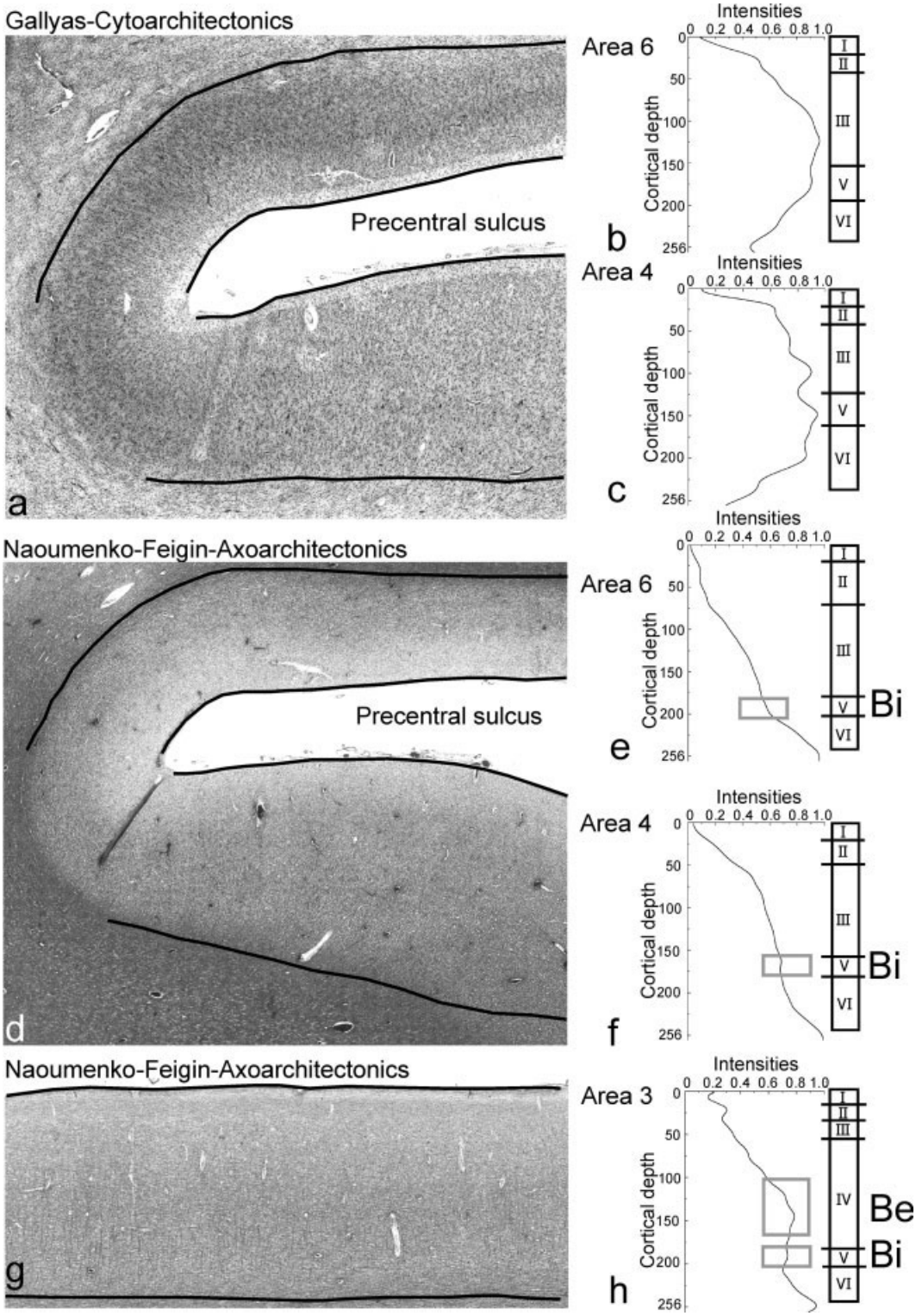

Fig. 7. The upper image (**a**) shows a mosaic of a section stained with the Merker modification of the Gallyas perikaryon stain. The region rostral to the precentral sulcus belongs to area 6 and has been delineated for generating traverses. The result of the averaged traverses is shown in the right profile diagram (**b**). The region occipital to the precentral sulcus is area 4 and has been delineated as well. The corresponding profile diagram is shown on the right side (**c**). An adjacent section was stained with the Naoumenko-Feigin stain to visualize axoarchitectonics (**d**). The corresponding profile diagrams are shown on the right side for area 6 (**e**) and area 4 (**f**). Since these agranular cortex regions are unistriate one stripe, the location of the inner stripe of Baillarger has been marked by (**Bi**). Image **g** shows the axoarchitectonic stained area 3 and its profile (**h**) with an outer stripe of Baillarger (**Be**) within lamina IV and an inner stripe of Baillarger (**Bi**) located in lamina V.

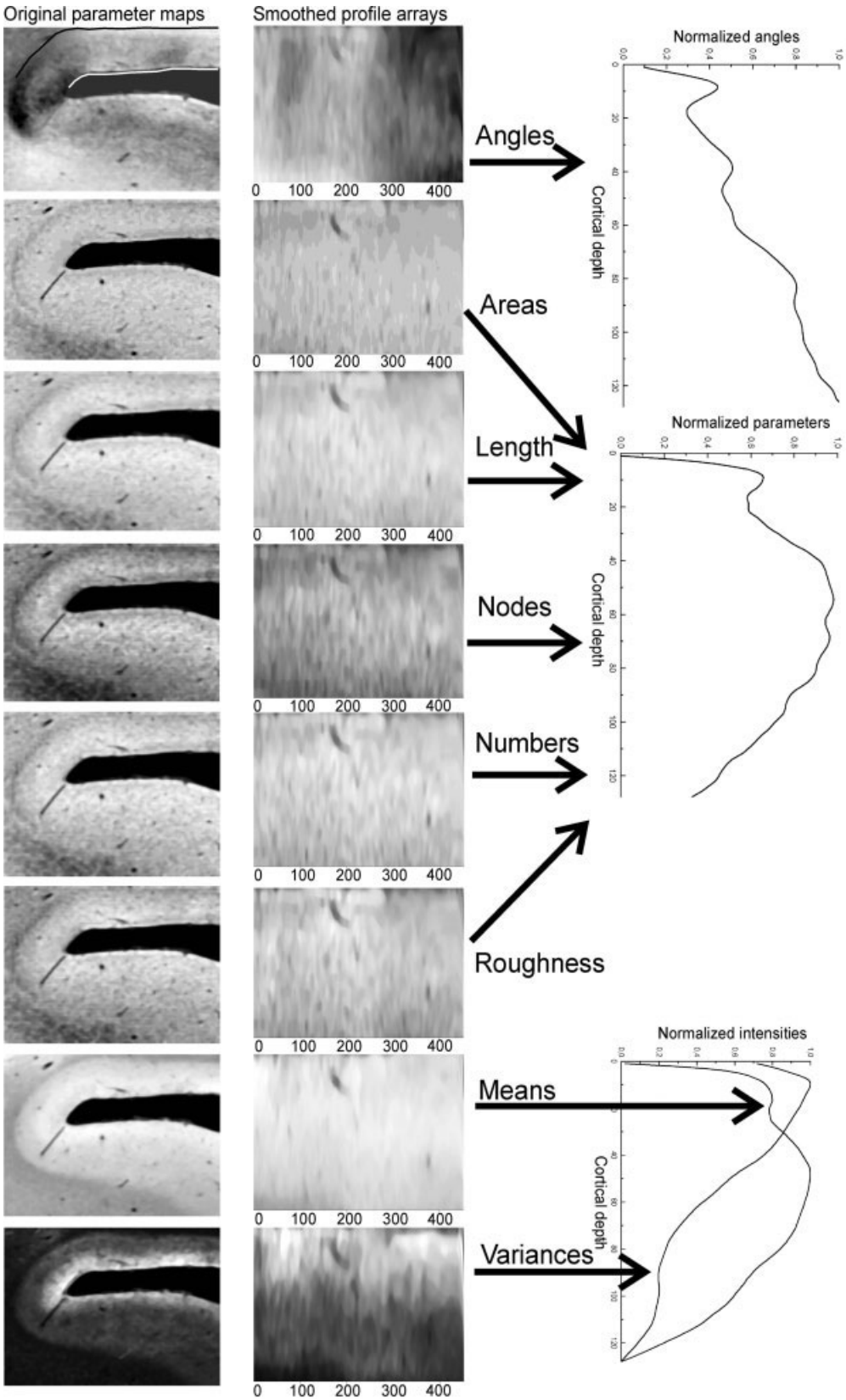

Fig. 8. These results were obtained from an analysis of area 4. The lower part of the cerebral cortex in the parameter maps belongs to area 4, as shown in Figure 7. Only this region was traversed to generate the profile arrays shown on the right side.

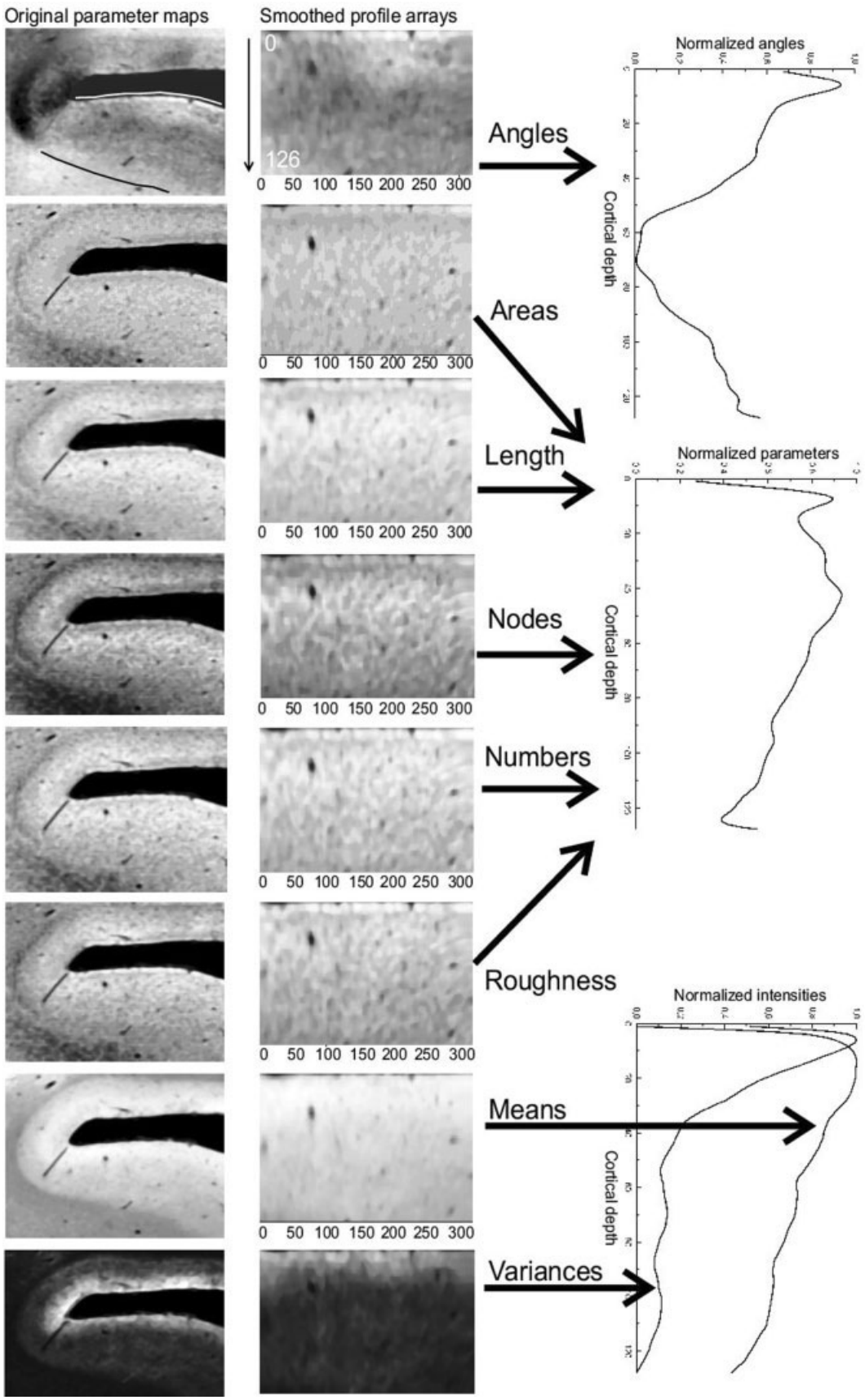

Fig. 9. The axoarchitectonic analysis of area 6 as delineated in 7 is documented here. In comparison to area 4 the averaged parameter profile curve in the middle is shifted more to the cortical surface.

Many horizontal fibers are found within layer I and these fiber orientations decrease strongly to layer II. Layer II can be characterized by oblique fiber orientations that are changing to more vertical orientations in layer III, correlating with massive perpendicular fiber bundles in this region; the orientations of axons become more oblique to the white matter border.

The mean gray value intensity profile shows an elongated and global peak within layers I and II. Staining intensity in this part of the cortical layering is strongest. The staining intensity decreases continuously down to the white matter border. The gray value variance of axons is large in layer I and decreases rapidly within layers II to III. One small and elongated subpeak within layers III to V and another one within layer VI indicate further changes of fibers gray value variance.

Morphometric and Densitometric Axon Parameters of Area 6. The most obvious difference of area 3 is that the global peak of the parameters located in the upper part of layer III and not in the upper part of layer III, as in area 4 (Fig. 9). In the deeper part of area 6 the profiles are decreasing more strongly than in area 4.

The profile of angles shows two pronounced peaks for oblique fibers in layer I and at the beginning of layer III (Fig. 9). Layer II is characterized by a further decrease of horizontal and oblique fibers courses.

The gray value variance curve shows a global peak in layers I and II followed by a decrease down to the white matter border. Only a small plateau can be observed within layer V. The mean gray value intensity shows also a wide peak over layers I and II, like the curve for area 4. The global peak of the mean gray values is located within layer III, decreasing thereafter to the white matter border.

Morphometric and Densitometric Axon Parameters of Area 3. The four morphometric parameters, area, length, number, and roughness, possess similar courses in area 3 (Fig. 10) as observed also in areas 4 and 6. The morphometric parameter curve indicates a peak over layer I to layer II, a decrease within layer II, and an increase in layer III. The global peak is located in layer IV. In layers V and VI to the white matter border only a small decrease can be observed. The distribution of axon angles shows a local peak at layers I and II for oblique courses. Then the curve increases strongly to layer IV, having a global peak there and indicating many horizontal axons. The density of horizontal axons decrease strongly down to the white matter border.

The global peak of the mean gray values is located within layers I and II. It decreases to layer IV, having in the deeper parts of layer IV a plateau and increasing slightly in layer VI. The mean gray value intensities shows a similar course as the variance; however, they exhibit a smoother distribution, resulting in missing subpeaks as those observed within the variance profile. The gray value variance of stained axons is largest within layer I, followed by a very strong decrease within layers II and III. A subpeak in layers III and IV can be observed. Furthermore, we found a relatively large subpeak in layer VI.

Fiber Analysis of Acetylcholinesterase (ACHE) in Area 6. Immunoreactive nerve fibers show a sufficient contrast for segmentation. Eight parameters of the fiber distribution are displayed in Figure 12. Those layers showing larger values of a parameter are demarked by a bar on the right side of each subfigure. In the orientation map, lower values mean ACHE-fiber-orientation more parallel to the pial surface respective to the other layers are located as a small band in the upper part of layer III just to the border to layer II. ACHE-fiber roughness shows larger values within layer II. The area, number, and length of ACHE-immunoreactive nerve fibers was found to be larger within the border of layers II–III. The largest values for branching of ACHE-positive nerve fibers were concentrated in the transition between layers II and III. The mean gray values of ACHE-immunoreactive nerve fibers were larger within layers II and III. However, the gray variance show large values within layers V and VI. The white matter in the gray variance map display comparable values as those in layers I and II. The roughness and area maps of immunoreactive nerve fibers show most clearly the white matter border.

Statistical Analysis of Parameter Maps. The parameter maps (Figs. 8, 9) of nerve fiber quantification of the histologic section through area 4 and area 6 were analyzed further to search for statistically significant structural changes along those pre- and primary motoric stripes.

The excess mass differences derived from the profile array containing all profiles of the delineated area 6 and area 4 (Fig. 11) were tested with the local rank test. For computational details and interpretation of diagrams, see Schmitt et al. (2003). Each parameter map (angles, area, length, mean, nodes, number, roughness, variance) were tested separately. Only those interval combinations are documented which show significant changes. Those significant differences that were found in different parameter maps in similar regions of the profile arrays were delineated by rectangles. Hence, five statistically significant ($P \leq 0.05$) zones marked by rectangles were found (Fig. 11), indicating a decrease (downward jump diagrams) or an increase (upward jump diagrams) of horizontal stratification of nerve fibers.

Accumulation of significant differences no. 1. This accumulation was detected in the downward jumps diagrams. The stratification pattern of fiber lengths, numbers, and nodes show an increase in this region just before the bottom of the precentral sulcus.

Accumulation of significant differences no. 2. The significant differences within various fiber maps (angle, area, length, mean, nodes, roughness) were located between profile numbers 500 and 600 in the downward jump diagrams. Exactly at this position the transition of area 6 to area 4 is located, as can easily be verified in the cytoarchitecture image mosaic in Figure 7, since in this cortical region giant pyramidal cells in layer V appear.

Accumulation of significant differences no. 3. The significant downward jumps were found between profile numbers 650 and 750. In this region the transition of subareas 4a and 4p is located.

Accumulation of significant differences no. 4. These statistical significations belong to a fold at the bottom

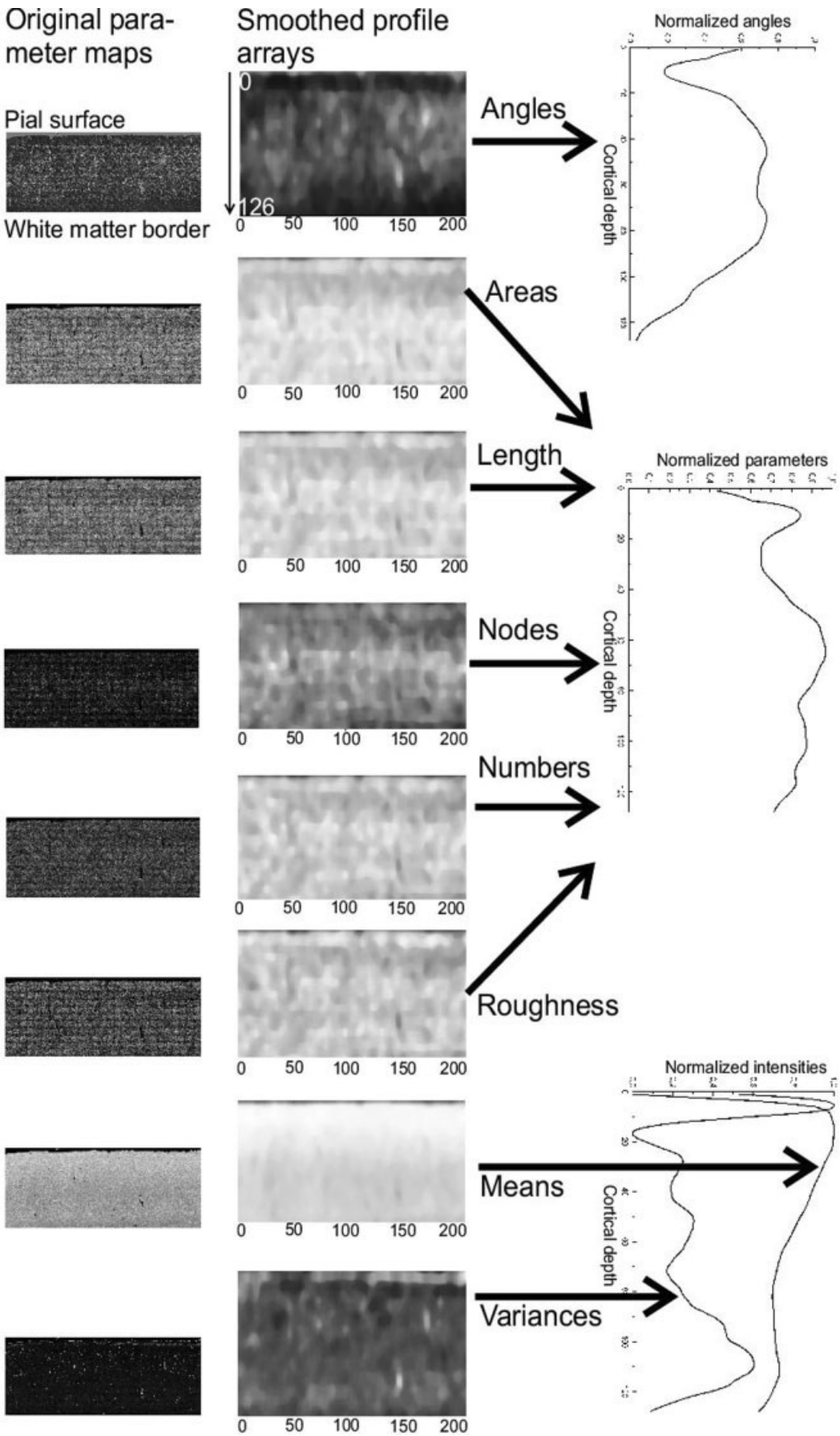
Original parameter maps
Smoothed profile arrays
Pial surface
White matter border
0
126
0 50 100 150 200
Angles
Areas
Length
Nodes
Numbers
Roughness
Means
Variances
Normalized angles
Normalized parameters
Normalized intensities
Cortical depth

Fig. 10.

of the precentral sulcus around profile no. 500. It produces a high significance in the upward jump diagram for the interval [1,2]. Hence, it does not contribute to a normal morphological change of fiber architecture.

Accumulation of significant differences no. 5. The last accumulation of significant differences was detected at profile no. 600 in the upward jump diagram. This means that larger profile peaks (excess masses of the first interval combinations) occur statistically significantly at this region, just behind the transition of area 4 to area 6.

The rostral beginning of this region is indicated by the accumulation of significant differences no. 1 described previously. Therefore, two transition zones are surrounding the bottom of the precentral sulcus and make it reasonable to demand a subarea at this location of area 6.

DISCUSSION

Theoretical Aspects of Axoarchitectonics

Numerous quantitative studies that investigate nerve fibers in the cerebral cortex aim to compare the basic scheme of horizontal myelin stratification in different areas (Braitenberg, 1962; Hopf, 1969, 1970; Hellwig, 1993; Hamano, 1996). However, myelin visualization by histologic or immunohistologic methods yields more or less clear macroscopic visualizations suitable for subdividing the cortex into disjunct areas and correlates them with cytoarchitectonic parcellations.

Thus far, nerve fiber quantification at the microscopic level was not performed. The topologic distributions of certain parameters that characterize axons are an important prerequisite for understanding axon distribution patterns. The data are useful for comparing the quantitative differences of brain areas of the same subject or between groups (age, sex, normal vs. pathologic). Data about axons and connectivity are the foundation of connectionist models or wiring models of brains (Mitchison, 1991; Cherniak, 1992, 1994, 1995; Young, 1996). Mainly, these models consider macrocircuits or connectivity between cortical areas and subcortical centers. One reason that we are not able so far to obtain data about spatial microconnectivity over whole brain areas is the lack of 3D information. However, even if such storage and computing resources exist for 3D-fiber-analysis the investigation of the third dimension would be restricted to the section thickness. Even the use of 3D confocal laser scanning microscopy (CLSM) would not provide a viable solution because CLSM is limited to a section thickness of ~400 μm (Pawley, 1995). Finally, the resulting parameter maps provide quantitative data that are necessary for modeling axonal sprouting, neuron modeling (Ascoli, 2001), and the simulation of nerve fiber distributions (Hellwig, 1993).

Overall, it was proven by visual inspection of the image mosaics, traversing and calculating area-specific averaged and normalized profiles, that the investigated areas belong to those Brodmann areas which were expected within preparation. After this preparative work the adjacent histologic sections stained by the method of Naoumenko-Feigin were investigated by the fiber analysis approach in order to characterize them in a quantitative manner.

The original image mosaics of a perikaryon stain (Gallyas-Merker) and an axon stain (Naoumenko-Feigin) were scanned by the traverse generating method (Schmitt and Böhme, 2002) to get averaged profiles of areas 3, 4, and 6. In the cytoarchitectonic profiles of area 4 and area 6 all five main layers (I, II, III, V, VI) were determined. In the average profiles of the axoarchitectonic image mosaics a unistriate type of cortex was found. This result correlates with the findings of others (Vogt, 1910; Strasburger, 1937; Hopf, 1956). However, in myelin stains the striation is more pronounced than in axoarchitectonic stained sections. In this study, myeloarchitectonics were not investigated because detailed information about topological changes of the structure of axons was intended to be analyzed. For this reason, such clear profiles for myeloarchitectonics (Braitenberg, 1962; Hopf, 1968b, 1969, 1970) were not found in the presented axoarchitectonic profiles.

Further studies need to be performed to better differentiate between axoarchitectonics and dendroarchitectonics, particularly by visualizing the relative specificity of axons and dendrites via immunohistochemical techniques. Axons can be specifically stained by incubating them with antibodies against PGP9.5 (Johnson et al., 1994) or SMI312 (Kirkcaldie et al., 2002), whereby microtubule-associated proteins (MAP2) (Matus, 2000) and SMI32 (Hof and Morrison, 1995; Arnold and Trojanowski, 1996) are concentrated in dendrites.

Profiles of Cytoarchitectonic and Axoarchitectonic Image Mosaics

In order to quantify, map, and statistically evaluate the axoarchitecture of the cerebral cortex, a method was developed that analyzes digital image tiles generated by a motorized videomicroscope at a magnification high enough for separating nerve fibers. It was demonstrated that the fiber analysis developed here can be applied to quantify different types of fibrillar distribution patterns (axoarchitectonic, fibrillar expression of immunohistochemical visualized acetylcholinesterase). The results of fiber analysis were transferred into normalized parameter maps. These maps were analyzed in order to get an overview of the principal distribution patterns. Such overviews are suitable for comparison of different parameter distributions within the same area as well as comparison within different areas. This was done for the cytoarchitectonic granular area 3 and the agranular areas 4 and 6.

Quantitative Axoarchitectonics

Structural inhomogeneities in the parameter maps may indicate different functional cortical fields. For cytoarchitectonic studies this was shown in numerous investigations (Geyer et al., 1996; Zilles et al., 1996;

Fig. 10. These parameter maps, profile arrays, and profile curves were derived from an area 3 analysis. The original parameter maps are shown in the left image column and the profile arrays in the middle. The profile arrays are generated form the Gaussian smoothed parameter maps. The averaged profile curve of the parameters are shown on the right. The curves of fiber areas, lengths, nodes, numbers, and roughness are averaged because they provide similar courses. The densitometric profiles of the mean gray values and their variances are shown at the bottom.

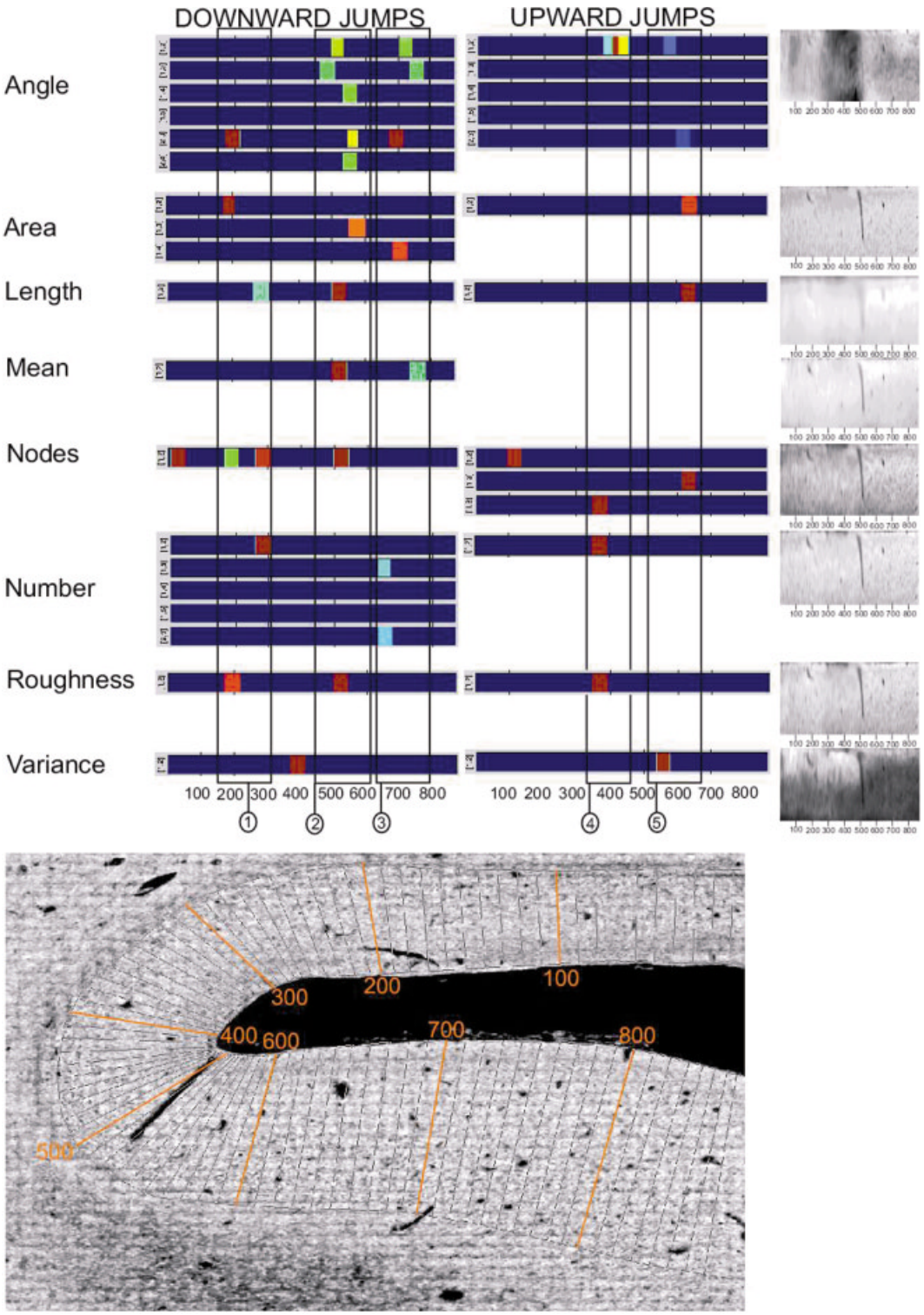

Fig. 11. The parameter maps of the whole region from the descending part of area 6 to the ascending part of area 4 was traversed in each parameter map. The resulting profile arrays were analyzed by the excess mass approach to calculate excess mass differences. These differences were statistically evaluated by the local rank test at $P \leq 0.01$. The frequency of significant differences is color-coded (red: highest frequency, and blue indicates less frequencies of significant differences at different scales). Each stripe, e.g., within the angle analysis, indicates an interval combination. For details, see Schmitt et al. (2003). Five suspicious regions were detected. Within these profile locations an accumulation of significant differences for different parameters was found. The accumulation marked by 2 is located at the transition region of area 6 to area 4 shown in the cytoarchitectonic map in Figure 7. The fourth accumulation can be related easily to the microfold. The significant upward jumps (increase of local peaks in the profiles) just before profile position 600 may indicate the subregion of area 4, as described in the text. [Color figure can be viewed in the online issue, which is available at www.interscience.wiley.com.]

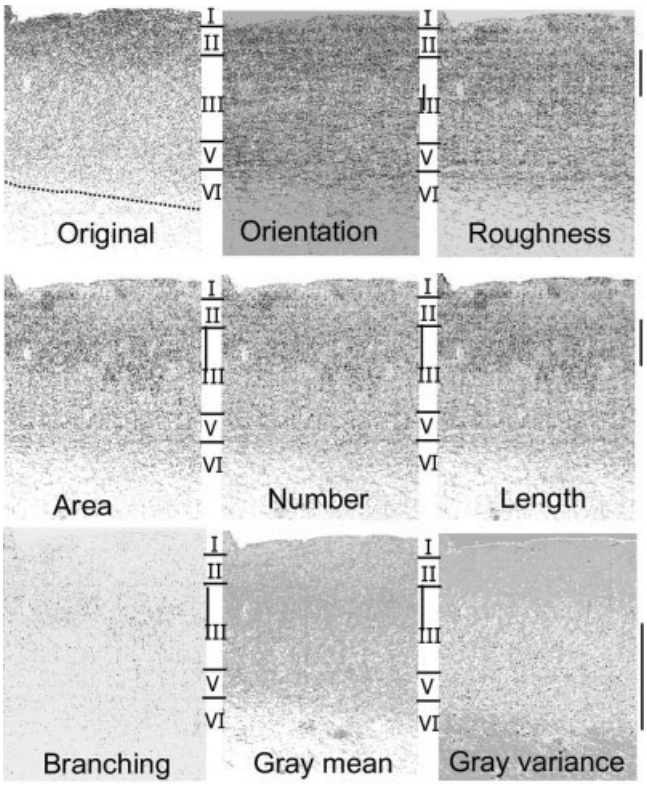

Fig. 12. The fiber analysis approach was also applied to immunohistochemical visualization of acetylcholine esterase of area 6. The major differences of the distribution pattern within each parameter map are indicated by lines on the right side of each parameter map. The original image mosaic is shown at the upper left corner.

Amunts et al., 1998; Grefkes et al., 2001). In the present study, the cerebral cortex was delineated in the parameter maps, and traverses within these areas were generated by an electrodynamic approach (Schmitt and Böhme, 2002). The resulting profile arrays of each parameter map were statistically evaluated by determining excess mass differences (Müller and Sawitzki, 1991; Schmitt and Böhme, 2002) by local rank testing (Dümbgen, 2002).

The comparison of the granular (area 3) and agranular (areas 4 and 6) cortices shows some remarkable differences. Lamina I of the agranular specimens contains a high degree of horizontal fibers, whereas these fibers in lamina I of area 3 are rare. The increase in more vertically oriented fibers within lamina III and lamina IV is large and decreases down to the white matter border. In contrast, areas 4 and 6 show an increase of vertical oriented fibers down to the white matter border. This observation within the angle parameter maps coincides with the functional projections of these areas, since an extensive projection from large and giant pyramidal cells of layers V and VI leave these areas.

Area 4 shows relatively more axons in layers II and III than area 6, indicated by a more convex course of the profile curve in Figure 7. This is a major axoarchitectonic difference between areas 4 and 6. The axoarchitectonic picture of area 3 is comparable with myeloarchitectonics insofar as a bistriate pattern can be recognized in the averaged profiles indicated by two peaks within layers IV and V (Fig. 7h). Areas 4 and 6 represent a further important difference due to their fiber orientation within lamina III. Area 4 has many fibers that are oriented horizontal and oblique but, on the other hand area 6 contains more vertical fibers. This situation changes at the ground of the precentral sulcus, where the concavity of the cerebral cortex is largest. In the cytoarchitectonic image mosaic, this region obviously belongs to area 6. However, fiber orientations undergo a dramatic change, since their horizontal and oblique orientations increase strongly, as indicated by low gray values in the parameter map of angles (Figs. 8, 9). Can this observation be explained by the geometry at the sulcus basin only; or may this change of orientation be an indicator of a functional subarea of area 6? Using structural features of these regions exclusively, we are not able to answer this question. A comparable situation was observed at the bottom of the central sulcus between area 4 and subarea 3b. Between these areas, subarea 3a is interposed at the basin of the central sulcus (Schmitt et al., 2003).

The granular and agranular specimens of the cerebral cortex show for all five remaining morphometric parameters similar profile patterns. Therefore, these profiles were averaged to obtain a single morphometric profile. The projections areas, lengths, branchings, numbers, and roughness increase from the cortical surface to layer II. The morphometric profile decreases and shows a local minimum within layer II. This local minimum is wider and reaches deeper into layer III of area 3. However, areas 4 and 6 contain a strong increase of the morphometric profile from layer II to layer V and a decrease down to the white matter border. In area 6 this decrease is steadier and steeper, whereas area 4 has a more elongated course of the profile and a strong decrease within layer VI. In area 3, a wide local maximum was detected within lamina IV and a local minimum at the transition from lamina IV to lamina V, followed by a further local maximum within lamina VI. In area 3 no such strong decrease of the morphometric profile was observed, indicating that interneuronal connectivity within these layers is strongly expressed. These morphometric parameters were determined and mapped here for the first time. However, there exist further relevant measures which provide reasonable information about axons. One important parameter is the mean thickness of axons. Naturally, this parameter is correlated with the projection area, but a directly measured value is necessary for inference of conductivity of nerve fibers. The mean thickness or diameter can be computed by the medial axes transform (Rosenfeld and Kak, 1982), but this is time-consuming and has to be optimized, although we hope to implement this soon. Furthermore, measures for convexity and concavity of fiber courses will be implemented in order to correlate theses quantities with intraareal and interareal types of projections. The angles of the orientation map can be classified into three different classes (vertical, horizontal, oblique) in order to obtain an overview of the principal orientations.

Finally, the densitometric maps of the gray level means and variance are compared. The granular area 3 shows a remarkable difference in comparison to the agranular cortices of areas 4 and 6. In all, the profiles

of the mean gray values are smoother than the variance profiles. The variance profile of area 3 shows, in comparison to areas 4 and 6, two local subpeaks: a wide one within layers II and III and a smaller one over layers V and VI. In area 3 layer IV is indicated in the profile of the mean staining intensities of the nerve fibers by a wide hollow that cannot be observed in the agranular area investigated here. This means that the staining intensity of nerve fibers within layer IV of area 3 is relatively larger than comparable depths of the agranular areas. In area 3 the variance profile shows a strong pronunciation of single layers not found in the agranular areas. The variance curves of the agranular areas show a relatively strong decrease with a final local peak within layer VI. This local peak of layer VI is strongly expressed in the variance profile of area 3. Comparing the variance profiles with that of area 4, a very strong decrease within layer III is found in area 6. The gray level distribution of nerve fibers within layers III to VI is more homogeneous in area 6 than in area 4. The mean staining intensity of nerve fibers in area 4 shows a wide global peak over layer III which is missing in area 6. Instead of this global peak, a relatively small and continuous decrease was found in area 6. The nerve fibers of layer III in area 4 show a very intensive staining that is larger than in the adjacent layers. Comparisons of the morphometric and the densitometric profiles of both agranular areas reveal that parameters seem to be more strongly expressed in the direction of the white matter border in area 4, suggesting that this location correlates with a strong projective motor function. Conversely, in area 6 these parameters are stronger expressed in the direction of the pial surface. This may indicate a stronger associative motor function of area 6, since interneuronal connections are located in the upper layers of the cerebral cortex.

Quantitative cortical mappings derived from histologic sections are always relatively perpendicular to the cortical surface. Therefore, tangential sections may influence the geometry of the parameter maps, and consequently the mean profile curves may change their observed features.

Further studies must be conducted in order to confirm our data using larger samples of serial sections. Such a serial pattern analysis should lead to comparable intersectional results by sequential statistical analysis.

Statistical Analysis of Axoarchitectonic Parameter Maps

It has been shown that the transition regions of areas 6 to 4 can be detected by analyzing the distribution of morphometric and densitometric parameters of nerve fibers. The results of the statistical evaluation have to be interpreted in relation to the underlying image mosaics in order to differentiate between artifacts and relevant structural inhomogeneities (Schmitt and Böhme, 2002). At present, however, it is impossible to automatically differentiate artifacts from physiological changes in axoarchitectonics or cytoarchitectonics. Therefore, the statistical evaluation of the parameter maps as well as any other kind of mapping derived from histologic image material can be only evaluated in terms of observer-supported transition region detection.

Thus, the statistical evaluation of the parameter maps of the precentral gyrus and the superior frontal gyrus were performed. Accumulations of significant differences over various parameter maps at comparable interval combinations (Schmitt et al., 2003) indicate structural-based changes of cortical functions which are related to interareal transition regions. It was observed that a transition region at the same profile position in all parameter maps appears, except for the number and the variance maps (Fig. 11). This suspect transition region was located just beneath the basin of the precentral sulcus close to the location of the image mosaic presenting the cytoarchitectonics. An artifact was detected by the statistical analysis as a significant increase of layering, too. However, this artifact, caused by a microfold straight through the cortex, can be detected and discriminated easily in the parameter maps as well as in the original nerve fiber image mosaics. Another interesting significant increase of stratification was found in the ascending part of area 4. This detected region can be related to the transition subarea of areas 4a and 4p (Geyer et al., 1996).

A further interesting observation was the appearance of a significant decrease of stratification before the basin of the precentral sulcus between profile positions 200 and 300 (Fig. 11). This could delineate the rostral part of a subregion of area 6. Further evidence is provided for this hypothesis by the parameter map of angles at the same position that shows a strong increase of horizontally located nerve fibers.

This evaluation scheme prevails in our current view of a basic organization of axoarchitectonics. We believe that this approach, while not definitive, will provide a useful framework for future investigation of the relation of structure and function of axoarchitectonics of the cerebral cortex.

SUMMARY

Discussion

Myeloarchitectonic stains provide a more pronounced pattern of striation; however, information about the microstructure of axons are obviously presented more clearly with the Naoumenko-Feigin procedure. An alternative technique to a histologic stain would be an immunohistochemical visualization of axons by more or less specific axonal markers like PGP 9.5 or SMI312. Especially, dendrites have not been visualized in this study, but would be of interest for structural mapping studies in the future.

The statistical approach applied here indicates different significant transition regions. Some of these transition regions are well known and were defined originally by cytoarchitectonic inhomogeneities. In addition to these generally known regions, subregions of the primary motoric cortex and, furthermore, a subdivision were detected in area 6 within the precentral sulcus.

The neuronal function of this transition region at the bottom of the precentral sulcus has to be investigated by in vivo methods and analysis of local receptor distributions. It is likely that these regions control specific or associative motoric tasks ([eye]-[finger, hand]-movement) because it is surrounded by motoric cortex regions.

Conclusion

The unistriate features of areas 3, 4, and 6 can be observed in axoarchitectonic stainings. The Naou-

menko-Feigin stain presents optimal results for quantitative evaluations. After applying videomicroscopic scanning for digitizing of histologic regions of interest, it is possible to calculate specific parameter maps that can be analyzed by traverse scanning and excess-mass statistics. We observed that morphometric as well as densitometric axon parameters increase in cortical depth in area 4 and reverse in the direction to the cortical surface in area 6. A subdivision of area 4 in areas 4a and 4p was found by statistical analysis of axoarchitectonic parameter maps. The analysis of area 6 indicates a subdivision in an anterior and posterior part.

Insofar as the aim of the present study was to establish an objective method for the appraisal of structural differences of nerve fibers, our axoarchitectonic quantification procedure appears to meet the purpose. Still unsolved are the problems concerning the spatial overlap of nerve fibers and their disappearance at the upper and lower surface of the sections. A 3D extension of the approach presented here and development of robust algorithms for spatial fiber tracing seems to be promising for the generation of neuronal wiring models based on real physical data.

ACKNOWLEDGMENTS

We thank U. Almert, P. Lau, E. Mecke of the Institute of Anatomy (University of Lübeck) for excellent histologic preparations, digitizing, and data administration; W. Kühnel (Institute of Anatomy, University of Lübeck) for extensive support; A. Wree (University of Rostock, Institute of Anatomy) for support and critical discussion; M. Westlund for editing the manuscript.

APPENDIX 1: Enhancement

In the following, basic definitions are given for closing and opening top-hat transformations that must be applied for a selective enhancement of thin curved structures like nerve fibers.

- *Dilatation* $\delta_B(A)$ for a gray level image A is a maximum-operator with a structuring element B as an operator frame (light objects will be enlarged, dark ones reduced):

$$\delta_B(A) := \max_{x \in B}\{x : x \in A\}.$$

- *Erosion* $\varepsilon_B(A)$ for a gray level image A is a minimum-operator with a structuring element B as an operator frame (dark objects will be enlarged, light ones reduced):

$$\varepsilon_B(A) := \min_{x \in B}\{x : x \in A\}.$$

- *Opening* $\phi_B(A)$ for a gray level image A with a structuring element B is an erosion followed by a dilation:

$$\phi_B(A) := \delta_B(\varepsilon_B(A)).$$

- *Closing* $\gamma_B(A)$ for a gray level image A with a structuring element B is a dilation followed by an erosion:

$$\gamma_B(A) := \varepsilon_B(\delta_B(A)).$$

- *Opening Top-Hat Transformation* $\Psi_B^{\phi}(A)$ for a gray level image A with a structuring element B is the difference between the image A and the closing operation (Fig. 4) (dark elongated objects are extracted):

$$\Psi_B^{\phi}(A) := A - \gamma_B(A).$$

- *Closing Top-Hat Transformation* $\Psi_B^{\gamma}(A)$ for a gray level image A with a structuring element B is the difference between the image A and the opening operation (light elongated objects are extracted):

$$\Psi_B^{\gamma}(A) := \phi_B(A) - A.$$

A suitable structuring element has to be chosen in order to detect long and thin structures which are not oriented preferentially in the images. Therefore, square and binary structure elements of the size k were applied:

$$B_k = (1)^{k,k}.$$

Cell nuclei can be suppressed by using a filter size of k = 9. Small as well as larger nerve fibers will be filtered at the given resolution. In order to reduce computation time, the maxima for the opening operation were calculated by rows and columns. Hence, $2(k - 1)$ comparisons per pixel instead of $k^2 - 1$ had to be computed (Pakura et al., 2002).

APPENDIX 2: Segmentation

The segmentation method of Otsu detects the optimal threshold of an image by maximizing the variance of gray level intensities between the two pixel classes C_0, for object pixels (foreground), and C_1, for nonobject pixels (background). The classes are separated by a gray level threshold s. Let L be the number of gray levels. Then all pixels with a value in $\{1,\ldots,s\}$ belong to C_0 and all pixels with a value in $\{s + 1,\ldots,L\}$ belong to C_1.

For the segmentation, the distribution of gray level values is analyzed (Fig. 4). Let p_i be the probability for a pixel to have the gray level value i, that is, p_i is the number of all pixels with value i divided by the number of pixels in the image. Then probabilities ω_0 and ω_1 for the classes C_0 and C_1 are:

$$\omega_0 = P\{C_0\} = \sum_{i=1}^{s} p_i = \omega(s),$$

$$\omega_1 = P\{C_1\} = \sum_{i=s+1}^{L} p_i = 1 - \omega(s).$$

In the above equation it has been used that $\omega_0 + \omega_1 = 1$. This follows from the fact that the p_i are the proba-

bility weights of a probability distribution. The class-averages μ_0 and μ_1 of both classes are given by:

$$\mu_0 = \sum_{i=1}^{s} iP\{i|C_0\} = \sum_{i=1}^{s} \frac{ip_i}{\omega_0} = \frac{\mu(s)}{\omega(s)}$$

and

$$\mu_1 = \sum_{i=s+1}^{L} iP\{i|C_1\} = \sum_{i=s+1}^{L} \frac{ip_i}{\omega_1} = \frac{\mu(L) - \mu(s)}{1 - \omega(s)},$$

where $\mu(L) = \sum_{i=1}^{s} ip_i$.

The average μ_L of the gray level distribution is:

$$\mu_L = \sum_{I=1}^{L} ip_i.$$

The two class variances are given by:

$$\sigma_0^2 = \sum_{i=1}^{s} (i - \mu_0)^2 P\{i|C_0\} = \sum_{i=1}^{s} \frac{(i - \mu_0)^2 p_i}{\omega_0},$$

$$\sigma_1^2 = \sum_{i=s+1}^{L} (i - \mu_1)^2 P\{i|C_1\} = \sum_{i=s+1}^{L} \frac{(i - \mu_1)^2 p_i}{\omega_1},$$

and the variance σ_L^2 of all gray values is:

$$\sigma_L^2 = \sum_{i=1}^{L} (i - \mu_L)^2 p_i.$$

The total variance σ_L^2 can be subdivided into an inner-class-variance σ_I^2 and an interclass-variance σ_Z^2:

$$\sigma_L^2 = \sigma_I^2 + \sigma_Z^2.$$

The innerclass-variance:

$$\sigma_I^2 = \omega_0\sigma_0^2 + \omega_1\sigma_1^2$$

is a weighted sum of the variances of each class, and the interclass-variance

$$\sigma_Z^2 = \omega_0(\mu_0 - \mu_L)^2 + \omega_1(\mu_1 - \mu_L)^2 = \omega_0\omega_1(\mu_1 - \mu_0)^2$$

is the weighted variance of the class-means around the overall mean.

Note that the total variance is independent of s, whereas the innerclass-variance and the interclass-variance depend on s. Thus, in order to maximize the variance between classes, either σ_I^2 has to be minimized or σ_Z^2 has to be maximized. Maximizing the interclass-variance σ_Z^2 is preferred, because here only the class-means have to be computed for each possible threshold, whereas for σ_I^2 the class-variances have to be computed.

Hence, the optimal threshold s^* is:

$$s^* = \operatorname*{argmax}_{1 \le s < L} \sigma_Z^2(s).$$

.

APPENDIX 3: Orientation

When a signal *s(x,y)* is oriented ideally in a certain region *G*, there exists an orientation in the *(x,y)*-plane along which *s(x,y)* in *G* does not change, whereas in the direction perpendicular to that orientation, changes occur (Bigün and Granlund, 1987; Jähne, 1997).

The basic idea is to rotate the coordinate system *(x,y)* to the coordinate system *(x̂,ŷ)* such that the change along $\hat{x}$ is minimal (Fig. 3). The transformation equations:

$$\begin{aligned} x &= \hat{x}\cos\alpha - \hat{y}\sin\alpha \quad & y &= \hat{x}\sin\alpha + \hat{y}\cos\alpha \\ \hat{x} &= x\cos\alpha + y\sin\alpha \quad & y &= -x\sin\alpha + y\cos\alpha \end{aligned}$$

rotate the coordinate system by an angle α, and we get:

$$\begin{aligned} s(x, y) &= s(\hat{x}\cos\alpha - \hat{y}\sin\alpha, \hat{x}\sin\alpha + \hat{y}\cos\alpha) \\ &= s_\alpha(\hat{x}, \hat{y}). \end{aligned}$$

This coordinate-transformation is shown in Figure 1.

The change of a signal *s(x,y)* in the direction with the angle α corresponds to the variance:

$$Q(\alpha) = \int\int_{\hat{G}} \left(\frac{\partial}{\partial\hat{x}} s_\alpha(\hat{x}, \hat{y})\right)^2 d\hat{x}d\hat{y}$$

of the signal in the region $G(x,y) = \hat{G}(\hat{x},\hat{y})$. When we express $Q(\alpha)$ in terms of *s(x,y)* we get:

$$\begin{aligned} Q(\alpha) &= \int\int_G \left(\frac{\partial}{\partial\hat{x}} s(x, y)\right)^2 dxdy \\ &= \int\int_G \left(s_x(x, y)\frac{\partial x}{\partial\hat{x}} + s_y(x, y)\frac{\partial y}{\partial\hat{x}}\right)^2 dxdy \\ &= \int\int_G (s_x(x, y)\cos\alpha + s_y(x, y)\sin\alpha)dxdy \\ &= \int\int_G (s_x^2(x, y)\cos^2\alpha + s_y^2(x, y)\sin^2\alpha \\ &\qquad + s_x(x, y)s_y(x, y)2\cos\alpha\sin\alpha)dxdy \\ &= \int\int_G (s_x^2(x, y)\cos^2\alpha + s_y^2(x, y)\sin^2\alpha \\ &\qquad + s_x(x, y)s_y(x, y)\sin(2\alpha))dxdy \end{aligned}$$

$$= \cos^2\alpha \underbrace{\int\int_G s_x^2(x,y)dxdy}_{J_{yy}} + \sin^2\alpha \underbrace{\int\int_G s_y^2(x,y)dxdy}_{J_{xx}}$$
$$+ \sin(2\alpha) \underbrace{\int\int_G s_x(x,y)s_y(x,y)dxdy}_{J_{xy}}$$
$$= \cos^2\alpha J_{yy} + \sin^2\alpha J_{xx} + \sin(2\alpha)J_{xy}.$$

Let $\alpha_0 = \text{argmin}\{Q(\alpha)\}$ be the orientation for which the variance is minimal. The necessary condition for the calculation of the minimum of $Q(\alpha)$ is the zero point of its first derivative, which is:

$$\begin{aligned} 0 &\overset{!}{=} \frac{\partial}{\partial\alpha} Q(\alpha_0) \\ &= -2\cos\alpha_0 \sin\alpha_0 J_{yy} + 2\sin\alpha_0 \cos\alpha_0 J_{xx} \\ &\quad + 2\cos(2\alpha_0)J_{xy} \\ &= -\sin(2\alpha_0)J_{yy} + \sin(2\alpha_0)J_{xx} + 2\cos(2\alpha_0)J_{xy} \\ &= \sin(2\alpha_0)(J_{xx} - J_{yy}) + 2\cos(2\alpha_0)J_{xy}. \end{aligned}$$

After reordering the equation the orientation α_0 can be computed as follows:

$$\tan(2\alpha_0) = \frac{\sin(2\alpha_0)}{\cos(2\alpha_0)} = \frac{2J_{xy}}{J_{yy} - J_{xx}}.$$

To estimate the reliability of the calculated orientation, the eigenvalues λ_1 and λ_2, where $\lambda_1 \geq \lambda_2$, of the symmetric inertia matrix:

$$T = \begin{pmatrix} J_{xx} J_{xy} \\ J_{xy} J_{yy} \end{pmatrix}$$

are considered. The eigenvectors of the inertia matrix are the principal axes along which $s(x,y)$ varies in the region $G(x,y)$. The eigenvalues are the lengths of these vectors. Hence, there are basically four possible situations:

- When $\lambda_1 > 0$ and $\lambda_2 = 0$ there exists an optimal orientation.
- When $\lambda_1 = \lambda_2 = 0$ the region has a constant gray value.
- When both values are greater than 0, then the gray value will change in all directions and no optimal orientation exists.
- A special case of the latter situation occurs when both eigenvalues have the same value. Then we have an isotropic structure (Jähne, 1997). In the present context this is a crossing of nerve fibers ("X").

The eigenvectors of symmetric matrices are orthogonal. T has the eigenvectors:

$$e_\alpha = \begin{pmatrix} \cos\alpha_0 \\ \sin\alpha_0 \end{pmatrix} \quad \text{and} \quad e_n = \begin{pmatrix} -\sin\alpha_0 \\ \cos\alpha_0 \end{pmatrix}.$$

Therefore, we get:

$$\begin{bmatrix} \cos\alpha_0 \sin\alpha_0 \\ -\sin\alpha_0 \cos\alpha_0 \end{bmatrix} \cdot \begin{bmatrix} J_{xx} J_{xy} \\ J_{xy} J_{yy} \end{bmatrix} \cdot \begin{bmatrix} \cos\alpha_0 - \sin\alpha_0 \\ \sin\alpha_0 \cos\alpha_0 \end{bmatrix} = \begin{bmatrix} \lambda_1 & 0 \\ 0 & \lambda_2 \end{bmatrix}.$$

Thus, the eigenvalues are:

$$\lambda_1 = J_{xx}\cos^2\alpha_0 + J_{yy}\sin^2\alpha_0 - J_{xy}\sin 2\alpha_0,$$
$$\lambda_2 = J_{xx}\sin^2\alpha_0 + J_{yy}\cos^2\alpha_0 + J_{xy}\sin 2\alpha_0.$$

To classify the orientation the coherence:

$$K = \left(\frac{\lambda_1 - \lambda_2}{\lambda_1 + \lambda_2}\right)^2 = \frac{(J_{yy} - J_{xx})^2 + 4J_{xy}^2}{(J_{xx} + J_{yy})^2}$$

is calculated. Obviously, K is in [0, 1]. For an ideal orientation, $\lambda_1 > 0$ and $\lambda_2 = 0$, it follows that $K = 1$. If the gray value is constant then $K = 0$, and if we have an isotropic structure $K \approx 0$.

In order to apply the derivatives and integrals to images they must be discretized. The directional derivatives $s_x(x,y)$ and $s_y(x,y)$ are approximated by the finite differences:

$$s_x(m, n) = \frac{1}{2}(s(m+1, n) - s(m-1, n))$$

and

$$s_y(m, n) = \frac{1}{2}(s(m, n+1) - s(m, n-1)).$$

The integration over G is realized by convolving of $(s_x(m,n))^2$, $(s_y(m,n))^2$, and $(s_x(m,n)s_y(m,n))$ with a low-pass filter $h(m,n)$:

$$J_{xx}(k, l) = \sum_m \sum_n h(k-m, l-n)(s_y(m, n))^2$$

$$J_{yy}(k, l) = \sum_m \sum_n h(k-m, l-n)(s_x(m, n))^2$$

$$J_{xy}(k, l) = \sum_m \sum_n h(k-m, l-n)s_x(m, n)s_y(m, n).$$

Applying these discrete equations the orientations of nerve fibers $\alpha_0(m,n)$ and the coherences $K(m,n)$ can be calculated for each pixel (m,n).

REFERENCES

Amunts K, Istomin V, Schleicher A, Zilles K. 1995. Postnatal development of the human primary motor cortex: a quantitative cytoarchitectonic analysis. Anat Embryol 192:557–571.

Amunts K, Klingberg T, Binkofski F, Schormann T, Seitz R, Roland P, Zilles K. 1998. Location, asymmetry and variability of human areas 17 and 18. NeuroImage 7:8.

Amunts K, Schleicher A, Bürgel U, Mohlberg H, Uylings H, Zilles K. 1999. Broca's region revisited: cytoarchitecture and intersubject variability. J Comp Neurol 412:319–341.

Arcelli C, Cordella L, Levialdi S. 1980. More about a thinning algorithm. Electron Lett 16:51–53.

Arnold S, Trojanowski J. 1996. Human fetal hippocampal development. II. The neuronal cytoskeleton. J Comp Neurol 367:293–307.
Ascoli G, Krichmar J, Scorcioni R, Nasuto S, Senft S. 2001. Computer generation and quantitative morphometric analysis of virtual neurons. Anat Embryol 204:283–301.
Bailey P, von Bonin G. 1951. The isocortex of man. Urbana: University of Illinois Press.
Baillarger J. 1840. Recherches sur la structure de la couche corticale des circonvolutions du cerveau. Mém Acad Roy Med 8:149–183.
Batsch E-G. 1956. Die myeloarchitektonische Untergliederung des Isocortex parietalis beim Menschen. J Hirnforsch 2:225–258.
Bigün J, Granlund G. 1987. Optimal orientation detection of linear symmetry. Proc ICCV. p 433–438.
Braak H. 1980. Architectonics of the human telencephalic cortex. Studies of brain function. Berlin: Springer.
Braitenberg V. 1962. A note on myeloarchitectonics. J Comp Neurol 118:141–156.
Bürgel U, Schormann T, Schleicher A, Zilles K. 1999. Mapping of histologically identified long fiber tracts in human cerebral hemispheres to the MRI volume of a reference brain: position and spatial variability of the optic radiation. NeuroImage 10:489–499.
Burke R, Marks W. 2002. Some approaches to quantitative dendritic morphology. In Ascoli GA, editor. Computational neuroanatomy. Totowa, NJ: Humana Press. p 27–48.
Chang H. 1952. Cortical neurons with particular reference to the apical dendrites. Cold Spring Harbor Symposia on Quantitative Biology 17:189–202.
Cherniak C. 1992. Local optimization of neuron arbors. Biol Cybern 66:503–510.
Cherniak C. 1994. Component placement optimization in the brain. J Neurosci 14:2418–2427.
Cherniak C. 1995. Neuronal component placement. TINS 18:522–527.
Dougherty E. 1993. Mathematical morphology in image processing. New York: Marcel Dekker.
Dümbgen L. 2002. Application of local rank tests to nonparametric regression. J Nonparam Stat 14:511–537.
Foley J. 2000. Computer graphics: principles and practice. New York: Addison-Wesley.
Frotscher M. 1992. Application of the Golgi/electron microscopy technique for cell identification in immunocytochemical, retrograde labeling, and developmental studies of hippocampal neurons. Microsc Res Tech 23:306–323.
Gerhardt E. 1940. Die Cytoarchitektonik des Isocortex parietalis beim Menschen. J Psychol Neurol 49:367–419.
Geyer S, Ledberg A, Schleicher A, Kinomura S, Schormann T, Bürgel U, Klingberg T, Larsson J, Zilles K, Roland P. 1996. Two different areas within the primary motor cortex of man. Nature 382:805–807.
Geyer S, Schleicher A, Zilles K. 1997. The somatosensory cortex of human: cytoarchitecture and regional distributions of receptor-binding sites. NeuroImage 6:27–45.
Geyer S, Matelli M, Luppino G, Schleicher A, Jansen Y, Palomero-Gallagher N, Zilles K. 1998. Receptor autoradiographic mapping of the mesial motor and premotor cortex of the macaque monkey. J Comp Neurol 397:231–250.
Geyer S, Schleicher A, Zilles K. 1999. Areas 3a, 3b, and 1 of human primary somatosensory cortex. 1. Microstructural organization and interindividual variability. NeuroImage 10:63–83.
Giardina C, Dougherty E. 1988. Morphological methods in image and signal processing. Englewood Cliffs, NJ: Prentice Hall.
Grefkes C, Geyer S, Schormann T, Roland P, Zilles K. 2001. Human somatosensory area 2: observer-independent cytoarchitectonic mapping, interindividual avariability, and population map. NeuroImage 14:617–631.
Hamano K. 1996. A quantitative analysis of rat central nervous system myelination using the immunohistochemical method for MBP. Dev Brain Res 93:18–22.
Hellwig B. 1993. How the myelin picture of the human cerebral cortex can be computed from cytoarchitectural data. A bridge between von Economo and Vogt. J Hirnforsch 34:387–402.
Hof P, Morrison J. 1995. Neurofilament protein defines regional patterns of cortical organization in the macaque monkey visual system: a quantitative immunohistochemical analysis. J Comp Neurol 352: 161–186.
Hopf A. 1956. Über die Verteilung myeloarchitektonischer Merkmale in der Stirnhirnrinde beim Menschen. J Hirnforsch 2:311–333.
Hopf A. 1966. Über eine Methode zur objektiven Registrierung der Myeloarchitektonik der Hirnrinde. J Hirnforsch 8:302–313.
Hopf A. 1968a. Photometric studies on the myeloarchitecture of the human temporal lobe. J Hirnforsch 10:285–297.
Hopf A. 1968b. Registration of the myeloarchitecture of the human frontal lobe with an extinction method. J Hirnforsch 10: 259–269.
Hopf A. 1969. Photometric studies on the myeloarchitecture of the human parietal lobe. I. Parietal region. J Hirnforsch 11:253–265.
Hopf A. 1970. Photometric studies on the myeloarchitecture of the human parietal lobe. II. Postcentral region. J Hirnforsch 12:135–141.
Jähne B. 1997. Digital image processing. Berlin: Springer. p 348–357.
Ji L, Piper J. 1992. Fast homotopy-preserving skeletons using mathematical morphology. IEEE PAMI 14:653–664.
Johnson P, Beggs J, Olafsen A, Watkins C. 1994. Unmyelinated nerve fiber estimation by immunocytochemistry. Correlation with electron microscopy. J Neuropathol Exp Neurol 53:176–183.
Kirkcaldie M, Dickson T, King C, Grasby D, Riederer B, Vickers J. 2002. Neurofilament triplet proteins are restricted to a subset of neurons in the rat neocortex. J Chem Neuroanat 24:163–171.
Landini G, Rippin J. 1996. How important is tumor shape? Quantification of the epithelial-connective tissue interface in oral lesions using local connected fractal dimension analysis. J Pathol 179:210–217.
Lashley K, Clark G. 1946. The cytoarchitecture of the cerebral cortex of Ateles: a critical examination of architectonic studies. J Comp Neurol 85:223–305.
Le Gros Clark W. 1952. A note on cortical cyto-architectonics. Brain 75:96–104.
Loyez M. 1910. Coloration des fibres nerveuses par la méthode à l'hématoxyline au fer après inclusion à celloidine. Compt Rend Soc Biol Paris 69:511–513.
Matus A. 2000. Actin-based plasticity in dendritic spines. Science 11:51–56.
Mitchison G. 1991. Neuronal branching patterns and the economy of cortical wiring. Proc R Soc Lond B 245:151–158.
Müller D, Sawitzki G. 1991. Excess mass estimates and tests for multimodality. J Am Stat Assoc 86:738–746.
Naoumenko J, Feigin K. 1967. A stable silver solution for axon staining in paraffin sections. J Neuropathol Exp Neurol 26:669–673.
Otsu N. 1979. A threshold selection method from gray-level histograms. IEEE Trans Systems Man Cyb 9:62–66.
Pakura M, Schmitt O, Aach T. 2002. Segmentation and analysis of nerve fibers in histologic sections of the cerebral human cortex. Proc 5th IEEE Southwest Symposium on Image Analysis and Interpretation, Santa Fe. p 1:62–66.
Pawley J. 1995. Handbook of biological confocal microscopy. New York: Plenum.
Rademacher J, Engelbrecht V, Bürgel U, Freund H-J, Zilles K. 1999. Measuring in vivo myelination of human white matter fiber tracts with magnetization transfer MR. NeuroImage 9:393–406.
Ráliš H, Beesley R, Ráliš Z. 1973. Techniques in neurohistology. London: Butterworths.
Ramon y Cajal S. 1911. Histologie du système nerveux de l'homme et des vertébrés, vol. II. Paris: A. Maloine. p 519–646.
Ristanović D, Nedeljkov V, Stefanović B, Milošević N, Štulić V. 2002. Fractal and nonfractal analysis of cell images: comparison and application to neuronal dendritic arborzation. Biol Cybern 87:278–288.
Romeis B. 1989. Mikroskopische Technik. München: Urban und Schwarzenberg.
Rosenfeld A, Kak AS. 1982. Digital picture processing, 2nd ed. New York: Academic Press.
Sanides F. 1962. Die Architektonik des menschlichen Stirnhirns. Monographien aus dem Gesamtgebiete der Neurologie und Psychiatrie: 98. Berlin: Springer.
Schmitt O, Böhme M. 2002. A robust transcortical profile scanner for generating 2D-traverses in histological sections of rich curved cortical courses. NeuroImage 16:1103–1119.
Schmitt O, Hömke L, Dümbgen L. 2003. Detection of cortical transition regions utilizing statistical analyses of excess masses. NeuroImage 19:42–63.
Serra J, Soille P. 1994. Mathematical morphology and its applications to image processing. Dordrecht: Kluwer.
Sholl D. 1956. The organization of the cerebral cortex. New York: John Wiley & Sons.
Somogyi H, Takagi P. 1982. A note on the use of picric acid-paraformaldehyde glutaraldehyde fixative for correlated light and electron microscopic immunocytochemistry. Neuroscience 7:1779–1783.
Strasburger E. 1937. Die myeloarchitektonische Gliederung des Stirnhirns beim Menschen und Schimpansen. J Psych Neurol 47: 461–491.

Tamura H. 1978. A comparison of line thinning algorithms from digital geometry viewpoint. Proc 4th IJCPR Kyoto 4:715–719.
van Oyen A, van Pelt J. 2002. Competition in neuronal morphogenesis and the development of nerve connection. In: Ascoli GA, editor. Computational neuroanatomy. Totowa, NJ: Humana Press. p 219–244.
Vogt O. 1910. Die myeloarchitektonische Felderung des menschlichen Stirnhirns. J Psychol Neurol 15:221–238.
Vogt O. 1911. Die Myeloarchitektonik des Isocortex parietalis. J Psychol Neurol 18:107–118.
Vogt C, Vogt O. 1919. Allgemeine Ergebnisse unserer Hirnforschung. J Psychol Neurol 25:279–461.
Young M. 1996. The analysis of cortical connectivity. Berlin: Springer.
Zilles K, Palomero-Gallagher N. 1999. Cyto-, myelo-, and receptor architectonics of the human parietal cortex. NeuroImage 14:8–20.
Zamperoni P. 1979. Methoden der digitalen Bildverarbeitung. Braunschweig: Vieweg.
Zamperoni P. 1991. Methoden der digitalen Bildverarbeitung. Braunschweig: Vieweg. p 121–131.
Zilles K, Gross G, Schleicher A, Schildgen S, Bauer A, Bahro M, Schwendemann G, Zech K, Kolassa N. 1991a. Regional and laminar distributions of α_1-adrenoceptors and their subtypes in human and rat hippocampus. Neuroscience 40:307–320.
Zilles K, Qü M, Schröder H, Schleicher A. 1991b. Neurotransmitter receptors and cortical architecture. J Hirnforsch 32:343–356.
Zilles K, Schlaug G, Matelli M, Luppino G, Schleicher A, Qu M, Dabringhaus A, Seitz R, Roland P. 1995. Mapping of human and macaque sensorimotor areas by integrating architectonic, transmitter receptor, MRI and PET data. J Anat 187:15–537.
Zilles K, Schlaug G, Geyer S, Luppino G, Matelli M, Schleicher A, Schormann T. 1996. Anatomy and transmitter receptors of the supplementary motor areas in the human and nonhuman primate brain. Adv Neurol 70:29–43.